Available online at www.sciencedirect.com
SCIENCE DIRECT®
Journal of Computational Physics 208 (2005) 493–526
JOURNAL OF COMPUTATIONAL PHYSICS
www.elsevier.com/locate/jcp

Application of dispersion-relation-preserving theory to develop a two-dimensional convection–diffusion scheme

R.K. Lin, Tony W.H. Sheu *

Department of Engineering Science and Ocean Engineering, National Taiwan University, No. 1, Sec. 4, Roosevelt Road, Taipei 106, Taiwan, Republic of China

Received 28 June 2004; received in revised form 23 February 2005; accepted 24 February 2005
Available online 14 April 2005

Abstract

In this paper a finite difference scheme is developed within the nine-point semi-discretization framework for the convection–diffusion equation. The employed Pade approximation renders a fourth-order temporal accuracy and the spatial approximation of convection terms accommodates the dispersion relation. The artificial viscosity introduced in the two-dimensional convection–diffusion-reaction (CDR) equation for stability reasons is analytically derived. Constraints on the mesh size and time interval for rendering a monotonic matrix are also rigorously derived. To validate the proposed method, we investigate several problems that are amenable to the exact solutions. The results with good rates of convergence are obtained for the investigated scalar and Navier–Stokes problems.

Keywords: Nine-point; Pade approximation; Fourth-order; Dispersion relation; Convection–diffusion-reaction equation; Monotonic

1. Introduction

A theoretically rigorous semi-discretization method for accurately solving the practically and academically important time-dependent convection–diffusion transport equation and Navier–Stokes equations is presented. For the time derivative term, Pade's approximation [1] is employed to render a fourth-order temporal accuracy. The remaining partial differential equation, which takes the convection–diffusion-reaction (CDR) form, involves only the spatial derivative terms. A reliable CDR scheme must have the ability to avoid convective instability problem for the convection dominated case. The theory adopted to minimize

* Corresponding author. Tel.: +886 2 33665791; fax: +886 2 23929885.
E-mail addresses: d89525003@ntu.edu.tw (R.K. Lin), twhsheu@ntu.edu.tw (T.W.H. Sheu).

0021-9991/$ - see front matter
doi:10.1016/j.jcp.2005.02.025

the dispersion error is to take the dispersive nature of the investigated partial differential equation into consideration [2].

A scheme used for the approximation of convection terms is called dispersion-relation-preserving (DRP) [2] if it accommodates the same dispersion relation as that of the original first-order partial derivative term. This relation, which is derived by taking the spatial Fourier transform of the first derivative term, reveals how the angular frequency relates with the wavenumber of the spatial variable [3]. The underlying reason of employing DRP convective scheme is that the dispersiveness, dissipation, group and phase velocities of each wave component supported by the first-order derivative can be well modelled [4]. In the above light, we combine the standard modified equation analysis, which involves truncated Taylor series, with the Fourier transform analysis [5], which enables us to derive the same or almost the same dispersion relation as the original partial differential equation, in the approximation of convective terms.

As many two-dimensional high-order convection–diffusion schemes show, the dispersion error, which is defined as the difference between the effective and actual wave numbers, cannot be completely eliminated using the presently developed two-dimensional DRP scheme. To enhance numerical stability we introduce the artificial viscosity into the semi-discretized equation to damp these non-resolved oscillations. For the sake of accuracy, we employ the general solution to the currently investigated two-dimensional transport equation for determining the introduced artificial viscosity.

This paper is organized as follows. Section 2 presents the working Navier–Stokes equations in primitive variable form. This is followed by applying the four-step Pade time stepping scheme [6]. The transient convection–diffusion equation can then be transformed into the steady-state convection–diffusion-reaction equation. In Section 4 the two-dimensional DRP scheme developed for the first-order derivative term is presented. A rigorous determination of artificial viscosity is also provided. Section 5 addresses the dispersion and Fourier (or von Neumann) stability analyses of the proposed discretization scheme. Section 6 presents the simulated results, from which the proposed two-dimensional conditionally monotonic convection–diffusion scheme is validated. In Section 7 we give concluding remarks.

2. Working equations

In this study we investigate the viscous incompressible fluid flow, which is governed by the following continuity equation and the Navier–Stokes equations for the chosen primitive variables $(\mathbf{u}, p)$:

$$\nabla \cdot \mathbf{u} = 0, \tag{2.1}$$

$$\frac{\partial \mathbf{u}}{\partial t} + (\mathbf{u} \cdot \nabla)\mathbf{u} = -\nabla p + \frac{1}{Re}\nabla^2 \mathbf{u} + \mathbf{f}. \tag{2.2}$$

The velocity vector $\mathbf{u}$ and pressure p are sought subject to the initial divergence-free velocity field and the boundary velocity. The length is scaled by L, the velocity components by U, the time by L/U, and the pressure by ρU^2, where ρ denotes the fluid density. The Reynolds number Re shown in (2.2) is the consequence of the above normalization.

Momentum equations can be directly solved together with the constraint equation (2.1). While fluid incompressibility can be unconditionally ensured, the eigenvalues of the resulting matrix system becomes poorly distributed. Convergent solutions for $(\mathbf{u}, p)$ are very difficult to obtain using the computationally less expensive iterative solver [7]. Very often, the peripheral storage required for the matrix equations may exceed the available computer power and disk space. These drawbacks prompt use of the pressure Poisson equation (PPE) approach [8] to overcome difficulty encountered in the mixed formulation. In this manner, the following Poisson equation for p is derived to replace Eq. (2.1) by applying a curl operator on Eq. (2.2):

$$\nabla^2 p = \nabla\left[-\frac{\partial \mathbf{u}}{\partial t} + \frac{1}{Re}\nabla^2\mathbf{u} - (\mathbf{u}\cdot\nabla)\mathbf{u} + \mathbf{f}\right]. \tag{2.3}$$

The above approach is not without complication since the elliptic system of equations is subject to a computationally more challenging integral boundary condition [9]. For this reason, we adopt the following Neumann-type pressure boundary condition:

$$\frac{\partial p}{\partial n} = \left[-\frac{\partial \mathbf{u}}{\partial t} + \frac{1}{Re}\nabla^2\mathbf{u} - (\mathbf{u}\cdot\nabla)\mathbf{u} + \mathbf{f}\right]\cdot\mathbf{n}. \tag{2.4}$$

In the above, **n** denotes the unit outward normal vector to the domain boundary.

3. Fourth-order accurate semi-discretization scheme

We consider the following model equation for ϕ due to its close resemblance to each momentum equation shown in (2.2):

$$\phi_t + a\phi_x + b\phi_y - k\nabla^2\phi = f, \tag{3.1}$$

where a and b denote the x- and y-direction velocities, respectively. Let $F(\equiv f - a\phi_x - b\phi_y + k\nabla^2\phi)$ be sufficiently differentiable, Eq. (3.1) can be rewritten as $\phi_t = F(\phi)$. In contrast to the method of lines, we begin with approximating the time derivative term ϕ_t. By expanding ϕ^{n+1} in Taylor series with respect to ϕ^n at $t = n\Delta t$, it is trivial to have $\phi^{n+1} = (1 + \Delta t\frac{\partial}{\partial t} + \frac{(\Delta t)^2}{2!}\frac{\partial^2}{\partial t^2} + \frac{(\Delta t)^3}{3!}\frac{\partial^3}{\partial t^3} + \cdots)\phi^n$. By virtue of $\exp(\tau) = 1 + \tau + \frac{1}{2!}\tau^2 + \frac{1}{3!}\tau^3 + \cdots$, ϕ^{n+1} can be exactly expressed as

$$\phi^{n+1} = \exp(\tau)\phi^n, \tag{3.2}$$

where $\tau = \Delta t\frac{\partial}{\partial t}$. In this study we apply the following fourth-order accurate Pade approximation [1] for $\exp(\tau)$:

$$\exp(\tau) = \frac{1 + \frac{1}{2}\tau + \frac{1}{12}\tau^2}{1 - \frac{1}{2}\tau + \frac{1}{12}\tau^2}. \tag{3.3}$$

Substitution of Eq. (3.3) into (3.2) yields

$$\left[1 - \frac{\tau}{2}\left(1 - \frac{1}{6}\tau\right)\right]\phi^{n+1} = \left[1 + \frac{\tau}{2}\left(1 + \frac{1}{6}\tau\right)\right]\phi^n. \tag{3.4}$$

Using $\phi^{n+\frac{1}{6}} = (1 + \frac{\tau}{6})\phi^n$ and $\tau = \Delta t\frac{\partial}{\partial t}$ allows us to derive $\phi^{n+\frac{1}{6}} = \phi^n + \frac{\Delta t}{6}\phi_t^n$. Scheme development is followed by employing $\phi^{n+\frac{1}{2}} = \phi^n + \frac{\tau}{2}\phi^{n+\frac{1}{6}}$ and $\phi^{n+\frac{5}{6}} = (1 - \frac{\tau}{6})\phi^{n+1}$ to derive

$$\phi^{n+\frac{1}{2}} = \phi^n + \frac{\Delta t}{2}\phi_t^{n+\frac{1}{6}}, \tag{3.5}$$

$$\phi^{n+\frac{5}{6}} = \phi^{n+1} - \frac{\Delta t}{6}\phi_t^{n+1}. \tag{3.6}$$

Eqs. (3.4) and (3.5) are then combined to derive

$$\left[1 - \frac{\tau}{2}\left(1 - \frac{\tau}{6}\right)\right]\phi^{n+1} = \phi^{n+\frac{1}{2}}. \tag{3.7}$$

By virtue of (3.6), the above equation can be rewritten as

$$\phi^{n+1} - \frac{\Delta t}{2}\phi_t^{n+\frac{5}{6}} = \phi^{n+\frac{1}{2}}. \tag{3.8}$$

In summary, the following two explicit and two implicit equations constitute the Pade scheme for the passive scalar ϕ [6]:

$$\phi^{n+\frac{1}{6}} = \phi^n + \frac{\Delta t}{6}F^n, \tag{3.9}$$

$$\phi^{n+\frac{1}{2}} = \phi^n + \frac{\Delta t}{2}F^{n+\frac{1}{6}}, \tag{3.10}$$

$$\frac{\Delta t}{6}F^{n+1} - \phi^{n+1} = -\phi^{n+\frac{5}{6}}, \tag{3.11}$$

$$\frac{\Delta t}{2}F^{n+\frac{5}{6}} - \phi^{n+1} = -\phi^{n+\frac{1}{2}}. \tag{3.12}$$

The calculation steps are given below:

(1) Calculate $\phi^{n+\frac{1}{6}}$ according to Eq. (3.9)

$$\phi^{n+\frac{1}{6}} = \phi^n + \frac{\Delta t}{6}\left(f^n - a\phi_x^n - b\phi_y^n + k\nabla^2\phi^n\right). \tag{3.13}$$

(2) Calculate $\phi^{n+\frac{1}{2}}$ according to Eqs. (3.10) and (3.13)

$$\phi^{n+\frac{1}{2}} = \phi^n + \frac{\Delta t}{2}\left(f^{n+\frac{1}{6}} - a\phi_x^{n+\frac{1}{6}} - b\phi_y^{n+\frac{1}{6}} + k\nabla^2\phi^{n+\frac{1}{6}}\right). \tag{3.14}$$

(3) Guess ϕ^{n+1} according to

$$\phi^{n+1} = \phi^n + \Delta t\left(f^n - a\phi_x^n - b\phi_y^n + k\nabla^2\phi^n\right). \tag{3.15}$$

(4) Calculate $\phi^{n+\frac{5}{6}}$ implicitly from Eq. (3.12) using the updated values of $\phi^{n+\frac{1}{2}}$ and ϕ^{n+1}

$$\left(a\phi_x^{n+\frac{5}{6}} - b\phi_y^{n+\frac{5}{6}} + k\nabla^2\phi^{n+\frac{5}{6}}\right)\Delta t = f^{n+\frac{5}{6}}\Delta t + 2\left(\phi^{n+\frac{1}{2}} - \phi^{n+1}\right). \tag{3.16}$$

(5) Calculate ϕ^{n+1} implicitly from

$$\left(a\phi_x^{n+1} + b\phi_y^{n+1} - k\nabla^2\phi^{n+1}\right)\Delta t + 6\phi^{n+1} = f^{n+1}\Delta t + 6\phi^{n+\frac{5}{6}}. \tag{3.17}$$

(6) Substitute ϕ^{n+1} into Eq. (3.16) to obtain $\phi^{n+\frac{5}{6}}$. This is followed by substituting $\phi^{n+\frac{5}{6}}$ into (3.17) to obtain ϕ^{n+1}. The above procedures are repeated until the L_2-norm of the computed difference between the consecutive iterations is less than the user's specified tolerance (10^{-15} is chosen in this study).

4. Discretization of spatial terms

As Eq. (3.17) reveals, the efficacy of the proposed semi-discretization scheme for Eq. (3.1) depends on the solution quality for the following convection–diffusion-reaction equation

$$\overline{a}\phi_x + \overline{b}\phi_y - \overline{k}\nabla^2\phi + \overline{c}\phi = \overline{f}. \tag{4.1}$$

In the above, $(\overline{a},\overline{b},\overline{k},\overline{c},\overline{f}) = (a\Delta t, b\Delta t, k\Delta t, 0, f^{n+\frac{5}{6}}\Delta t + 2(\phi^{n+\frac{1}{2}} - \phi^{n+1}))$ and $(a\Delta t, b\Delta t, k\Delta t, 6, f^{n+1}\Delta t + 6\phi^{n+\frac{5}{6}})$ for Eqs. (3.16) and (3.17), respectively. For simplicity, Eq. (4.1) is solved subject to the prescribed boundary solution $\phi = \mathbf{g}$.

4.1. Optimum dispersion-relation-preserving scheme for the first-order derivative term

The first-order spatial derivative terms shown in (4.1) will be approximated in the nine-point grid system schematic in Fig. 1. Take ϕ_x as an example, it can be approximated as follows for the case of $\Delta x = \Delta y = h$

$$\phi_x(x,y) \approx \frac{1}{h}(a_1\phi_{i-1,j-1} + a_2\phi_{i,j-1} + a_3\phi_{i+1,j-1} + a_4\phi_{i-1,j} + a_5\phi_{i,j} + a_6\phi_{i+1,j} + a_7\phi_{i-1,j+1} + a_8\phi_{i,j+1} + a_9\phi_{i+1,j+1}). \tag{4.2}$$

We apply the Taylor series expansion method for $\phi_{i\pm1,j}$, $\phi_{i,j\pm1}$, $\phi_{i\pm1,j\pm1}$ to eliminate the leading eight error terms shown in the resulting modified equation. Eliminating coefficients for ϕ, ϕ_x, ϕ_y, ϕ_{xx}, ϕ_{xy}, ϕ_{yy}, ϕ_{xxy} and ϕ_{xyy} allows us to derive the following algebraic equations:

$$a_1 + a_2 + a_3 + a_4 + a_5 + a_6 + a_7 + a_8 + a_9 = 0, \tag{4.3}$$
$$-a_1 + a_3 - a_4 + a_6 - a_7 + a_9 = 1, \tag{4.4}$$
$$-a_1 - a_2 - a_3 + a_7 + a_8 + a_9 = 0, \tag{4.5}$$
$$a_1 + a_3 + a_4 + a_6 + a_7 + a_9 = 0, \tag{4.6}$$
$$a_1 - a_3 - a_7 + a_9 = 0, \tag{4.7}$$
$$a_1 + a_2 + a_3 + a_7 + a_8 + a_9 = 0, \tag{4.8}$$
$$-a_1 - a_3 + a_7 + a_9 = 0, \tag{4.9}$$
$$-a_1 + a_3 - a_7 + a_9 = 0, \tag{4.10}$$

One more equation is needed for the unique determination of coefficients a_i ($i = 1,2,\ldots,9$) shown in (4.2).

As convection highly dominates diffusion, approximation of ϕ_x by the standard truncated Taylor series is not necessarily logical from the propagation point of view. Instead, how to preserve the dispersion relation, which signifies the functional relation between the angular frequency of the wave and the

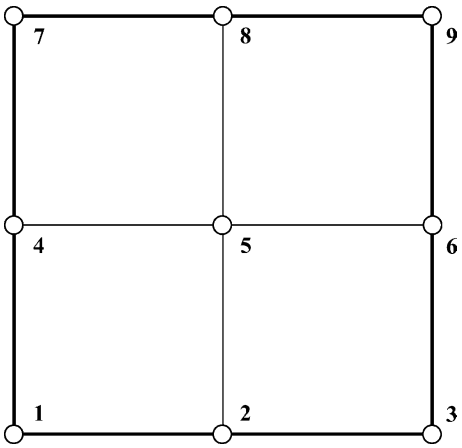

Fig. 1. Schematic of the nine stencil points.

wavenumber of the spatial variable for ϕ_x, becomes crucial to suppress the possible convective instability in the approximation of ϕ_x [10]. The right-hand side of (4.2) is, thus, desirable to have nearly the same Fourier transform in space as the original partial derivative term shown in the left-hand side of Eq. (4.2). Following the DRP method [2,11], which has been applied with success to approximate ϕ_x within the one-dimensional context, define the Fourier transform and its inverse for $\phi(x,y)$ in two space dimensions as follows:

$$\tilde{\phi}(\alpha,\beta) = \frac{1}{(2\pi)^2}\int_{-\infty}^{+\infty}\int_{-\infty}^{+\infty}\phi(x,y)\mathrm{e}^{-\mathbf{i}(\alpha x+\beta y)}\,\mathrm{d}x\,\mathrm{d}y, \tag{4.11}$$

$$\phi(x,y) = \int_{-\infty}^{+\infty}\int_{-\infty}^{+\infty}\tilde{\phi}(\alpha,\beta)\mathrm{e}^{\mathbf{i}(\alpha x+\beta y)}\,\mathrm{d}\alpha\,\mathrm{d}\beta. \tag{4.12}$$

By applying the spatial Fourier transform to terms on both sides of (4.2), we are led to derive α in the actual wavenumber vector $\underline{\alpha} = (\alpha,\beta)$

$$\alpha \approx \frac{-\mathbf{i}}{h}\left(a_1\mathrm{e}^{-\mathbf{i}(\alpha h+\beta h)} + a_2\mathrm{e}^{-\mathbf{i}\beta h} + a_3\mathrm{e}^{\mathbf{i}(\alpha h-\beta h)} + a_4\mathrm{e}^{-\mathbf{i}\alpha h} + a_5 + a_6\mathrm{e}^{\mathbf{i}\alpha h} + a_7\mathrm{e}^{-\mathbf{i}(\alpha h-\beta h)} + a_8\mathrm{e}^{\mathbf{i}\beta h} + a_9\mathrm{e}^{\mathbf{i}(\alpha h+\beta h)}\right). \tag{4.13}$$

In view of the above equation, the right-hand side of (4.13) is defined as the effective wavenumber $\tilde{\alpha}$ in $\underline{\tilde{\alpha}} = (\tilde{\alpha},\tilde{\beta})$:

$$\tilde{\alpha} = \frac{-\mathbf{i}}{h}\left(a_1\mathrm{e}^{-\mathbf{i}(\alpha h+\beta h)} + a_2\mathrm{e}^{-\mathbf{i}\beta h} + a_3\mathrm{e}^{\mathbf{i}(\alpha h-\beta h)} + a_4\mathrm{e}^{-\mathbf{i}\alpha h} + a_5 + a_6\mathrm{e}^{\mathbf{i}\alpha h} + a_7\mathrm{e}^{-\mathbf{i}(\alpha h-\beta h)} + a_8\mathrm{e}^{\mathbf{i}\beta h} + a_9\mathrm{e}^{\mathbf{i}(\alpha h+\beta h)}\right), \tag{4.14}$$

where $\mathbf{i} = \sqrt{-1}$. Similarly, we can derive

$$\tilde{\beta} = \frac{-\mathbf{i}}{h}\left(b_1\mathrm{e}^{-\mathbf{i}(\alpha h+\beta h)} + b_2\mathrm{e}^{-\mathbf{i}\beta h} + b_3\mathrm{e}^{\mathbf{i}(\alpha h-\beta h)} + b_4\mathrm{e}^{-\mathbf{i}\alpha h} + b_5 + b_6\mathrm{e}^{\mathbf{i}\alpha h} + b_7\mathrm{e}^{-\mathbf{i}(\alpha h-\beta h)} + b_8\mathrm{e}^{\mathbf{i}\beta h} + b_9\mathrm{e}^{\mathbf{i}(\alpha h+\beta h)}\right). \tag{4.15}$$

Note that $\underline{\tilde{\alpha}}$ can be regarded as an approximation to $\underline{\alpha}$ in the sense that it is effectively the wavenumber of Fourier transform of the finite difference equation shown in the right-hand side of (4.2) [2].

To assure that the current Fourier transform of the finite-difference equation in (4.2) is a proper representation for ϕ_x over an adequate range of wavenumbers, we demand that α be close to $\tilde{\alpha}$. In the weak sense, $|\tilde{\alpha}h - \alpha h|^2$ (or the following integrated error E) should approach zero over a proper range of wave numbers [2,3,10]:

$$E(\alpha) = \int_{-\frac{\pi}{2}}^{\frac{\pi}{2}}\int_{-\frac{\pi}{2}}^{\frac{\pi}{2}}|\tilde{\alpha}h - \alpha h|^2\,\mathrm{d}(\alpha h)\,\mathrm{d}(\beta h) = \int_{-\frac{\pi}{2}}^{\frac{\pi}{2}}\int_{-\frac{\pi}{2}}^{\frac{\pi}{2}}|\mathbf{i}\tilde{\gamma_1} - \gamma_1|^2\,\mathrm{d}\gamma_1\,\mathrm{d}\gamma_2, \tag{4.16}$$

where $(\gamma_1,\gamma_2) = (\alpha h,\beta h)$. In the discrete system for ϕ_x, the modified wavenumber range should be adequate to define a period of sine (or cosine) wave. This explains why the integral range shown in (4.16) is chosen to be $-\frac{\pi}{2} \leqslant \gamma_1,\gamma_2 \leqslant \frac{\pi}{2}$. To make E a minimum value, we enforce the following equation:

$$\frac{\partial E}{\partial a_6} = 0. \tag{4.17}$$

Employing the above extreme condition at point 6 schematic in Fig. 1 enables us to obtain the nine introduced coefficients from Eqs. (4.17) and (4.3)–(4.10):

$$a_1 = a_3 = a_7 = a_9 = \frac{\pi}{4(\pi-2)}, \tag{4.18}$$

$$a_2 = a_8 = \frac{-\pi}{2(\pi-2)}, \tag{4.19}$$

$$a_4 = \frac{1-\pi}{\pi-2}, \tag{4.20}$$

$$a_6 = \frac{-1}{\pi-2}, \tag{4.21}$$

$$a_5 = \frac{\pi}{\pi-2}. \tag{4.22}$$

Note that $\tilde{\alpha} = \tilde{\alpha}(\alpha,\beta)$ evaluated at $\alpha = 0$ is equal to zero according to Eqs. (4.14) and (4.18)–(4.22). As for $\tilde{\alpha}(\alpha,0)$ and $\tilde{\alpha}(\alpha=\beta)$, their values are expressed as $\frac{1}{h}\sin(\gamma_1)$ and $\frac{1}{h}[\sin(\gamma_1) - \mathbf{i}(\frac{\pi}{2(\pi-2)}\cos(2\gamma_1) - \frac{2\pi}{\pi-2}\cos(\gamma_1) + \frac{3\pi}{2(\pi-2)})]$, respectively.

Based on the nine determined coefficients shown in (4.18)–(4.22), the modified equation for ϕ_x is shown to have the spatial accuracy order of two:

$$\phi_x = \frac{h^2}{6}\phi_{xxx} + \frac{\pi h^3}{4(\pi-2)}\phi_{xxyy} + \frac{h^4}{120}\phi_{xxxxx} + \cdots + \text{HOT}. \tag{4.23}$$

Similarly, the nine-point stencil approximation equation for $\phi_y (\approx \frac{1}{h}\sum_{i,j=-1}^{+1} b_k \phi(x+ih, y+jh);\ k = 1,2,\ldots,9)$ accommodates dispersion feature on conditions that $b_4 = b_6 = a_2$, $b_2 = a_4$, $b_8 = a_6$ and $b_j = a_j (j = 1,3,5,7,9)$. The modified equation for ϕ_y is $\phi_y = \frac{h^2}{6}\phi_{yyy} + \frac{\pi h^3}{4(\pi-2)}\phi_{xxyy} + \frac{h^4}{120}\phi_{yyyyy} + \cdots + \text{HOT}$.

To reveal that the proposed finite difference equation can approximate ϕ_x over the range of wavenumbers of interest, we plot in Fig. 2 the contour values of $|\tilde{\alpha}h - \alpha h|/\pi$, $|\tilde{\beta}h - \beta h|/\pi$ and $||\underline{\tilde{\alpha}}|h - |\underline{\alpha}|h|/\pi$ against (γ_1,γ_2). It is seen that only the small wave number components can be well resolved within the acceptable accuracy. Such scheme's inability prompts us to derive the artificial viscosity in Section 4.2 for suppressing the unresolved convective instability. We also plot in Fig. 3 the values of $\left|\frac{\tilde{\alpha}}{\alpha} - 1\right|$, $\left|\frac{\tilde{\beta}}{\beta} - 1\right|$ and $\left|\frac{|\underline{\tilde{\alpha}}|}{|\underline{\alpha}|} - 1\right|$ against (γ_1,γ_2) for showing the degree of unresolved dispersion errors.

The nine-point formula given in [12] will be employed to approximate $\phi_{xx} + \phi_{yy}$ in the Cartesian coordinate system with $\Delta x = \Delta y = h$:

$$\nabla^2\phi = 4(\phi_{i+1,j} + \phi_{i-1,j}) + 4(\phi_{i,j+1} + \phi_{i,j-1}) + (\phi_{i-1,j-1} + \phi_{i+1,j-1} + \phi_{i-1,j+1} + \phi_{i+1,j+1}) - 20\phi_{i,j}. \tag{4.24}$$

The modified equation for $\nabla^2\phi$ can be derived as

$$\nabla^2\phi = \frac{h^2}{12}(\phi_{xxxx} + 2\phi_{xxyy} + \phi_{yyyy}) + \cdots + \text{HOT}. \tag{4.25}$$

4.2. Development of a nodally exact artificial viscosity model

We consider the following two-dimensional model equation for Eqs. (3.16) and (3.17):

$$a\phi_x + b\phi_y - k\nabla^2\phi + c\phi = f. \tag{4.26}$$

For the sake of accuracy, the general solution given below for the above model equation is employed

$$\phi(x,y) = c_1 e^{\lambda_1 x} + c_2 e^{\lambda_2 x} + c_3 e^{\lambda_3 y} + c_4 e^{\lambda_4 y} + \frac{f}{c}, \tag{4.27}$$

where c_i $(i = 1,2,3,4)$ are four constants. By substituting Eq. (4.27) into Eq. (4.26), λ_1, λ_2, λ_3 and λ_4 shown above can be derived as

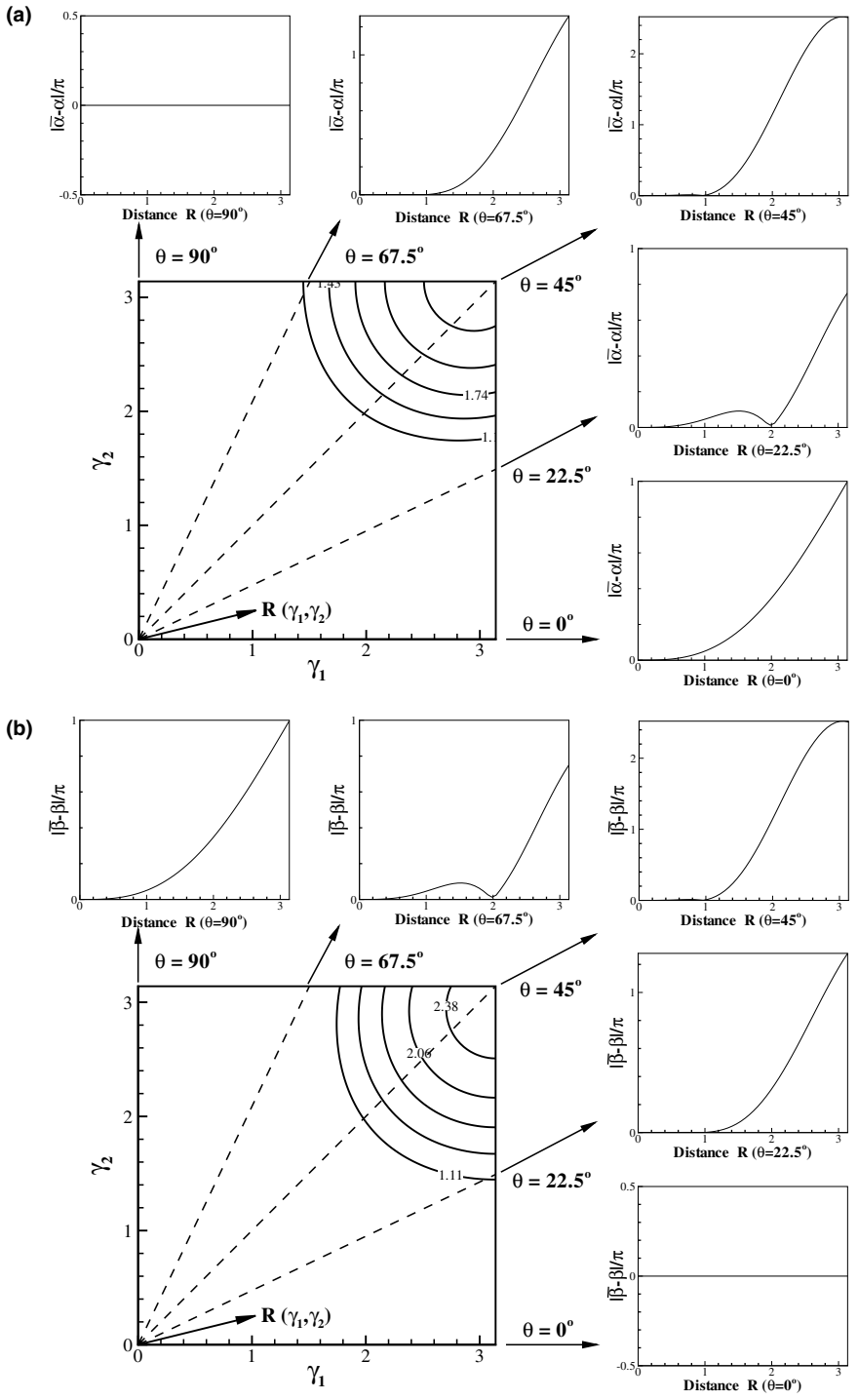

Fig. 2. Plots of the contour values for ϕ against (γ_1, γ_2), where ϕ are (a) $|\tilde{\alpha}h - \alpha h|/\pi$; (b) $|\tilde{\beta}h - \beta h|/\pi$; (c) $||\tilde{\underline{\alpha}}|h - |\underline{\alpha}|h|/\pi$.

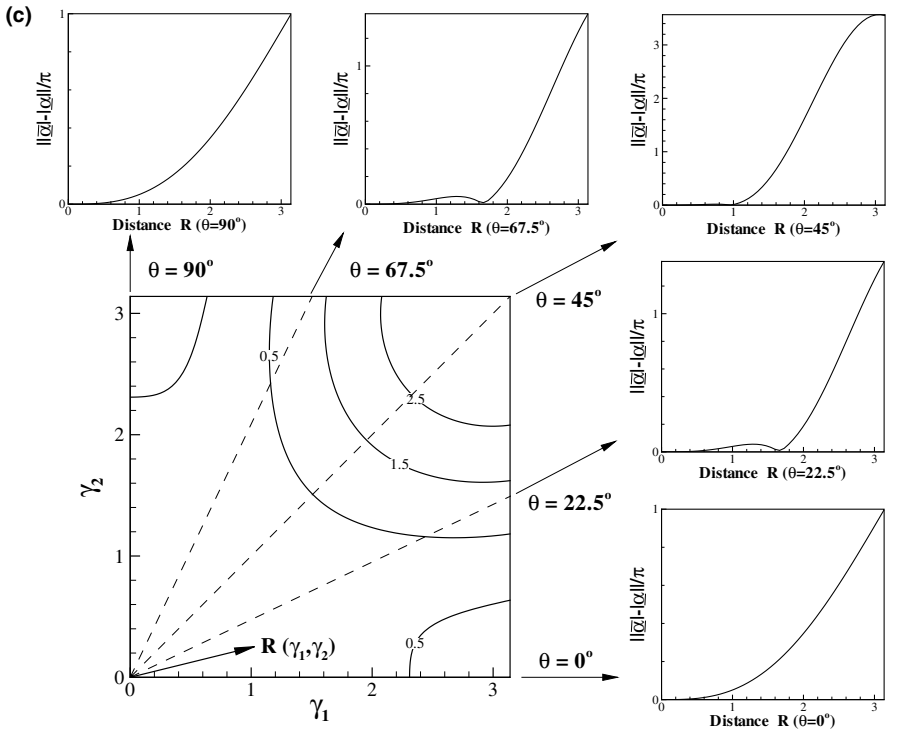

Fig. 2 (*continued*)

$$\lambda_{1,2} = \frac{a \pm \sqrt{a^2 + 4ck}}{2k} \quad \text{and} \quad \lambda_{3,4} = \frac{b \pm \sqrt{b^2 + 4ck}}{2k}. \tag{4.28}$$

To enhance convective stability, we introduced an artificial viscosity m to rewrite Eq. (4.26) as $a\phi_x + b\phi_y - (k+m)\nabla^2\phi + c\phi = f$. This is followed by substituting the exact solutions for $\phi_{i,j}$, $\phi_{i\pm1,j}$, $\phi_{i,j\pm1}$ and $\phi_{i\pm1,j\pm1}$ into the nine-point DRP equation to yield

$$A_1\phi_{i-1,j-1} + A_2\phi_{i,j-1} + A_3\phi_{i+1,j-1} + A_4\phi_{i-1,j} + A_5\phi_{i,j} + A_6\phi_{i+1,j} + A_7\phi_{i-1,j+1} + A_8\phi_{i,j+1} + A_9\phi_{i+1,j+1} = f. \tag{4.29}$$

Nine coefficients A_i ($i = 1,2,\ldots,9$) are derived in terms of $a_i (i = 1,2,\ldots,9)$ and $b_i (i = 1,2,\ldots,9)$, which take the same forms as a_i, given in (4.18)–(4.22) as

$$A_i = \frac{a_i a + b_i b}{h} - \frac{k+m}{h^2} + \frac{c}{28}, \quad i = 1,3,7,9, \tag{4.30}$$

$$A_j = \frac{a_j a + b_j b}{h} - \frac{4(k+m)}{h^2} + \frac{c}{14}, \quad j = 2,4,6,8, \tag{4.31}$$

$$A_5 = \frac{a_5 a + b_5 b}{h} + \frac{20(k+m)}{h^2} + \frac{4c}{7}. \tag{4.32}$$

The artificial viscosity m shown in (4.30)–(4.32) is expressed as

$$m = \frac{\frac{ah}{2}\sinh\overline{\lambda_1}\cosh\overline{\lambda_2} + \frac{bh}{2}\sinh\overline{\lambda_3}\cosh\overline{\lambda_4} + \frac{ch^2}{7}\left(\cosh\overline{\lambda_1}\cosh\overline{\lambda_2} + \cosh\overline{\lambda_3}\cosh\overline{\lambda_4} + 5\right)}{6\left(\cosh\overline{\lambda_1}\cosh\overline{\lambda_2} + \cosh\overline{\lambda_3}\cosh\overline{\lambda_4} - 2\right)} - k, \tag{4.33}$$

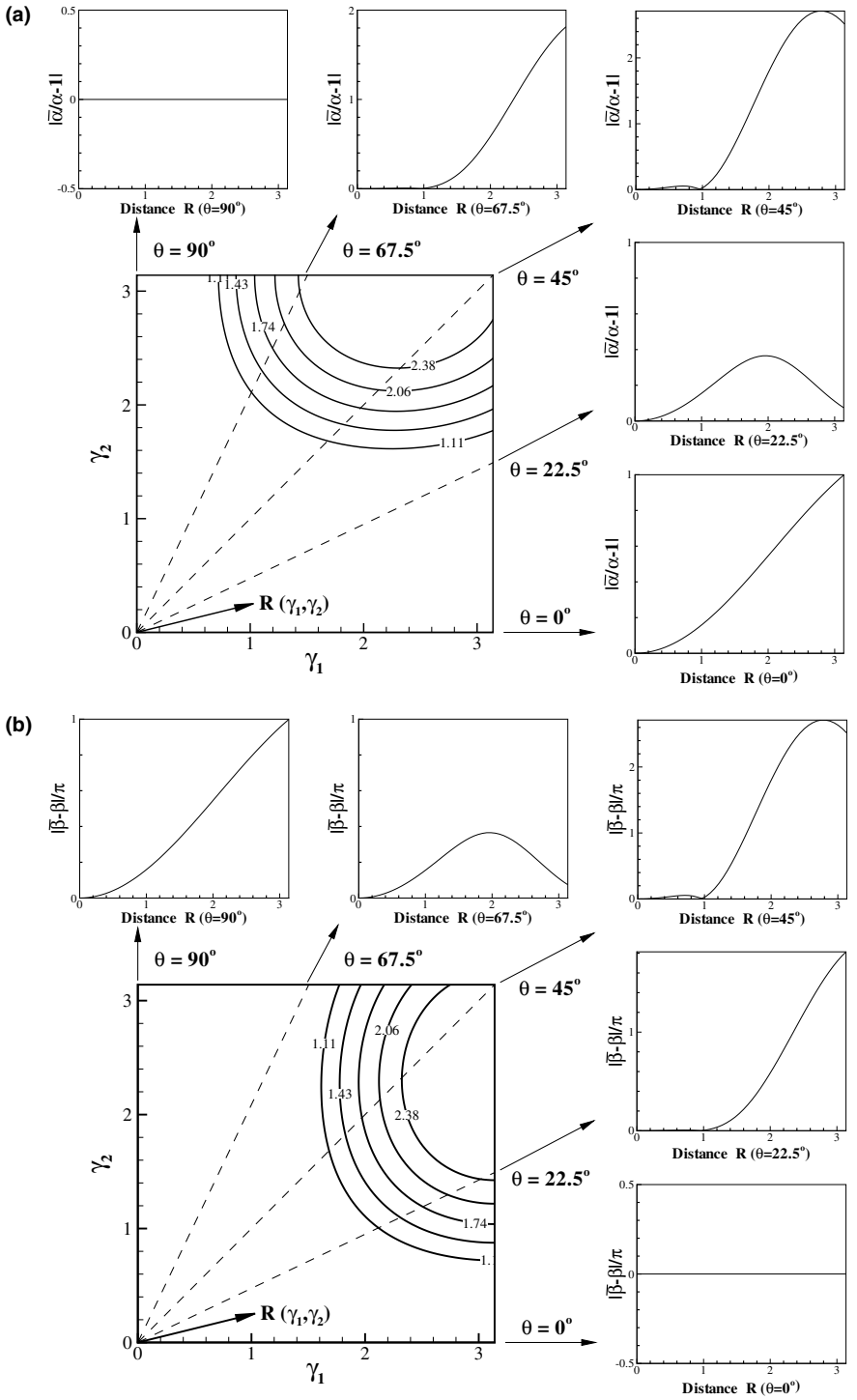

Fig. 3. Plots of the contour values for ϕ against (γ_1, γ_2), where ϕ are (a) $|\frac{\bar{\alpha}}{\alpha} - 1|$; (b) $|\frac{\bar{\beta}}{\beta} - 1|$; (c) $|\frac{|\bar{\alpha}|}{|\alpha|} - 1|$.

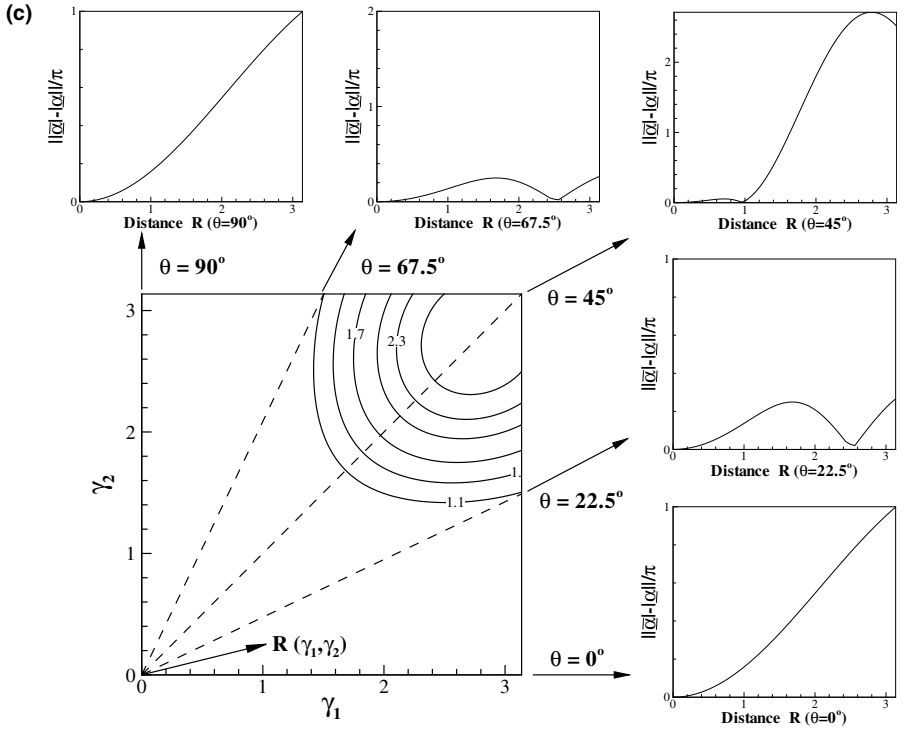

Fig. 3 (*continued*)

where $(\overline{\lambda_1}, \overline{\lambda_2}) = \left(\frac{ah}{2k}, \sqrt{\left(\frac{ah}{2k}\right)^2 + \frac{ch^2}{k}}\right)$ and $(\overline{\lambda_3}, \overline{\lambda_4}) = \left(\frac{bh}{2k}, \sqrt{\left(\frac{bh}{2k}\right)^2 + \frac{ch^2}{k}}\right)$. The modified equation for Eq. (4.26) can be derived as

$$a\phi_x + b\phi_y - k\nabla^2\phi + c\phi = \frac{ch^2}{7}\left(\phi_{xx} + \phi_{yy}\right) + \frac{h^2}{6}\left(a\phi_{xxx} + b\phi_{yyy}\right) + h^2\left(\frac{ch^2}{84} - \frac{k+m}{12}\right)\left(\phi_{xxxx} + \phi_{yyyy}\right) + h^2\left(\frac{ch^2}{28} + \frac{\pi(a+b)h}{2(\pi-2)} - \frac{k+m}{6}\right)\phi_{xxyy} + \frac{h^4}{120}\left(a\phi_{xxxxx} + b\phi_{yyyyy}\right) + \cdots + \text{HOT}. \tag{4.34}$$

5. Dispersion and Fourier (or von Neumann stability) analyses

Theoretical study of the proposed DRP scheme detailed in Sections 2 and 3 starts with adding Eqs. (3.11) and (3.12) together and then employing the definitions given in (3.9) and (3.10) to derive the equivalent one-step implicit equation

$$\phi^{n+1} = \frac{1}{2}\left(\phi^{n+\frac{1}{6}} + \phi^{n+\frac{5}{6}}\right) + \frac{\Delta t}{12}\left(F^{n+1} - F^n + 3F^{n+\frac{1}{6}} + 3F^{n+\frac{5}{6}}\right). \tag{5.1}$$

Given $\phi(x, y, t = 0) = \exp[\mathbf{i}(\alpha x + \beta y)]$, Eq. (3.1) with $f = 0$ can be easily shown to have the following exact solution:

$$\phi(x,y,t) = \exp\left\{-\left[k\left(\alpha^2+\beta^2\right)+c\right]t\right\}\exp\left\{\mathbf{i}[\alpha(x-at)+\beta(y-bt)]\right\}, \tag{5.2}$$

where (α,β) denotes the wavenumber vector. The discrete equation for (5.1) is expressed as follows by virtue of the definition given in $F(\phi)$ and the discretizations described in Section 4 for ϕ_x, ϕ_y and $\nabla^2\phi$

$$\sum_{i,j=-1}^{+1}\overline{A}_k\phi^{n+1}(x+ih,y+jh) = 6\left(\phi^{n+\frac{1}{6}}+\phi^{n+\frac{5}{6}}\right)+\sum_{i,j=-1}^{+1}\left[\overline{B}_k\phi^{n}(x+ih,y+jh)-3\overline{B}_k\phi^{n+\frac{1}{6}}(x+ih,y+jh)\right.$$
$$\left.-3\overline{B}_k\phi^{n+\frac{5}{6}}(x+ih,y+jh)\right],\quad k=1,2,\ldots,9, \tag{5.3}$$

where $(v_x,v_y)=(\frac{a\Delta t}{h},\frac{b\Delta t}{h})$ and

$$\overline{A}_i = \left(a_iv_x+b_iv_y\right)-\frac{1}{2}\left(\frac{v_x}{Pe_x}+\frac{v_y}{Pe_y}\right)-\overline{m}+\frac{v_xR_x+v_yR_y+12}{56},\quad i=1,3,7,9, \tag{5.4}$$

$$\overline{A}_j = \left(a_jv_x+b_jv_y\right)-2\left(\frac{v_x}{Pe_x}+\frac{v_y}{Pe_y}\right)-4\overline{m}+\frac{v_xR_x+v_yR_y+12}{28},\quad j=2,4,6,8, \tag{5.5}$$

$$\overline{A}_5 = \left(a_5v_x+b_5v_y\right)+10\left(\frac{v_x}{Pe_x}+\frac{v_y}{Pe_y}\right)+20\overline{m}+\frac{2(v_xR_x+v_yR_y+12)}{7}, \tag{5.6}$$

$$\overline{B}_i = \left(a_iv_x+b_iv_y\right)-\frac{1}{2}\left(\frac{v_x}{Pe_x}+\frac{v_y}{Pe_y}\right)+\frac{v_xR_x+v_yR_y}{56},\quad i=1,3,7,9, \tag{5.7}$$

$$\overline{B}_j = \left(a_jv_x+b_jv_y\right)-2\left(\frac{v_x}{Pe_x}+\frac{v_y}{Pe_y}\right)+\frac{v_xR_x+v_yR_y}{28},\quad j=2,4,6,8, \tag{5.8}$$

$$\overline{B}_5 = \left(a_5v_x+b_5v_y\right)+10\left(\frac{v_x}{Pe_x}+\frac{v_y}{Pe_y}\right)+\frac{2(v_xR_x+v_yR_y)}{7}. \tag{5.9}$$

In the above, $\overline{m}$ is expressed as

$$\overline{m} = \frac{\frac{v_x}{2}\sinh\overline{\lambda_1}^*\cosh\overline{\lambda_2}^*+\frac{v_y}{2}\sinh\overline{\lambda_3}^*\cosh\overline{\lambda_4}^*}{6\left(\cosh\overline{\lambda_1}^*\cosh\overline{\lambda_2}^*+\cosh\overline{\lambda_3}^*\cosh\overline{\lambda_4}^*-2\right)}-\frac{1}{2}\left(\frac{v_x}{Pe_x}+\frac{v_y}{Pe_y}\right)$$
$$+\frac{\frac{v_xR_x+v_yR_y+12}{14}\left(\cosh\overline{\lambda_1}^*\cosh\overline{\lambda_2}^*+\cosh\overline{\lambda_3}^*\cosh\overline{\lambda_4}^*+5\right)}{6\left(\cosh\overline{\lambda_1}^*\cosh\overline{\lambda_2}^*+\cosh\overline{\lambda_3}^*\cosh\overline{\lambda_4}^*-2\right)}, \tag{5.10}$$

where $(Pe_x,Pe_y)=(\frac{ah}{k},\frac{bh}{k})$, $(R_x,R_y)=(\frac{ch}{a},\frac{ch}{b})$, $(\overline{\lambda_1}^*,\overline{\lambda_2}^*)=(\frac{Pe_x}{2},\sqrt{(\frac{Pe_x}{2})^2+Pe_xR_x})$ and $(\overline{\lambda_3}^*,\overline{\lambda_4}^*)=(\frac{Pe_y}{2},\sqrt{(\frac{Pe_y}{2})^2+Pe_yR_y})$. For completeness, we plot in Fig. 4 the contour values of $\frac{\overline{m}}{k}$ against (v_x,v_y) at $R_x=R_y=0$, $Pe_x=Pe_y=2,\ 10,\ 10^3,\ 10^4$.

Due to the inevitable amplitude and phase errors, the exact solution for the proposed finite difference equation (3.1) is assumed to take the following form:

$$\tilde{\phi}(x,y,t) = \exp\left\{-\left[\left(k\alpha^2+\frac{c}{2}\right)\frac{k_r}{\gamma_1^2}+\left(k\beta^2+\frac{c}{2}\right)\frac{k_r}{\gamma_2^2}\right]t\right\}\exp\left\{\mathbf{i}\left[\alpha\left(x-a\frac{k_i}{\gamma_1}t\right)+\beta\left(y-b\frac{k_i}{\gamma_2}t\right)\right]\right\}. \tag{5.11}$$

As already defined in Section 4.1, $(\gamma_1,\gamma_2)=(\alpha h,\beta h)$. Dispersion analysis of the discrete equation for (3.1) involves substituting $\phi_{i,j}$, $\phi_{i\pm1,j}$ and $\phi_{i,j\pm1}$, which are obtained from Eq. (5.11), into Eq. (3.1). After some algebra, k_r and k_i accounting for the respective amplitude and phase errors are derived as

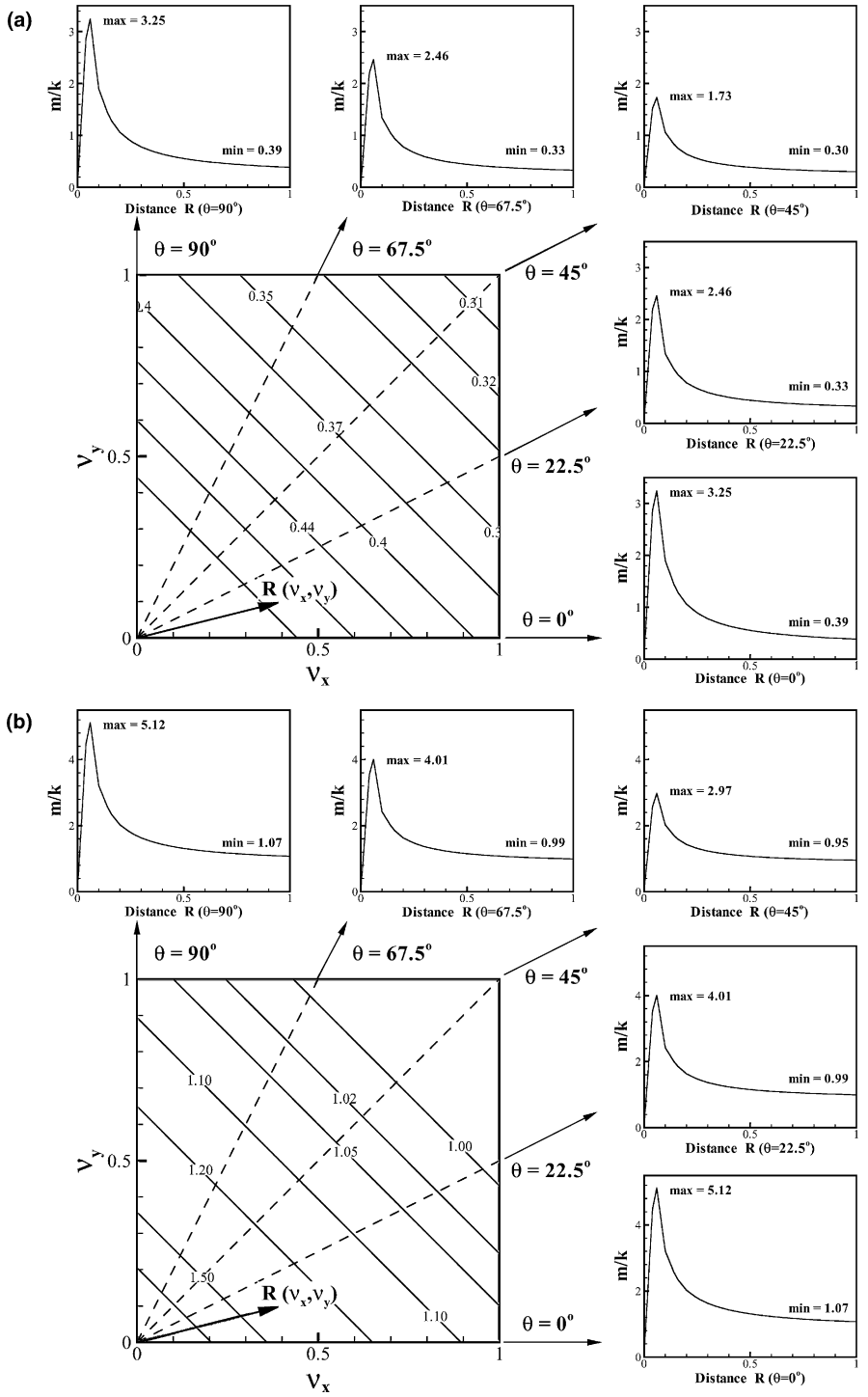

Fig. 4. Plots of the ratio $\frac{m}{k}$ against the Courant numbers (v_x, v_y) at $R_x = R_y = 0$ and (a) $Pe_x = Pe_y = 2$; (b) $Pe_x = Pe_y = 10$; (c) $Pe_x = Pe_y = 10^2$; (d) $Pe_x = Pe_y = 10^3$.

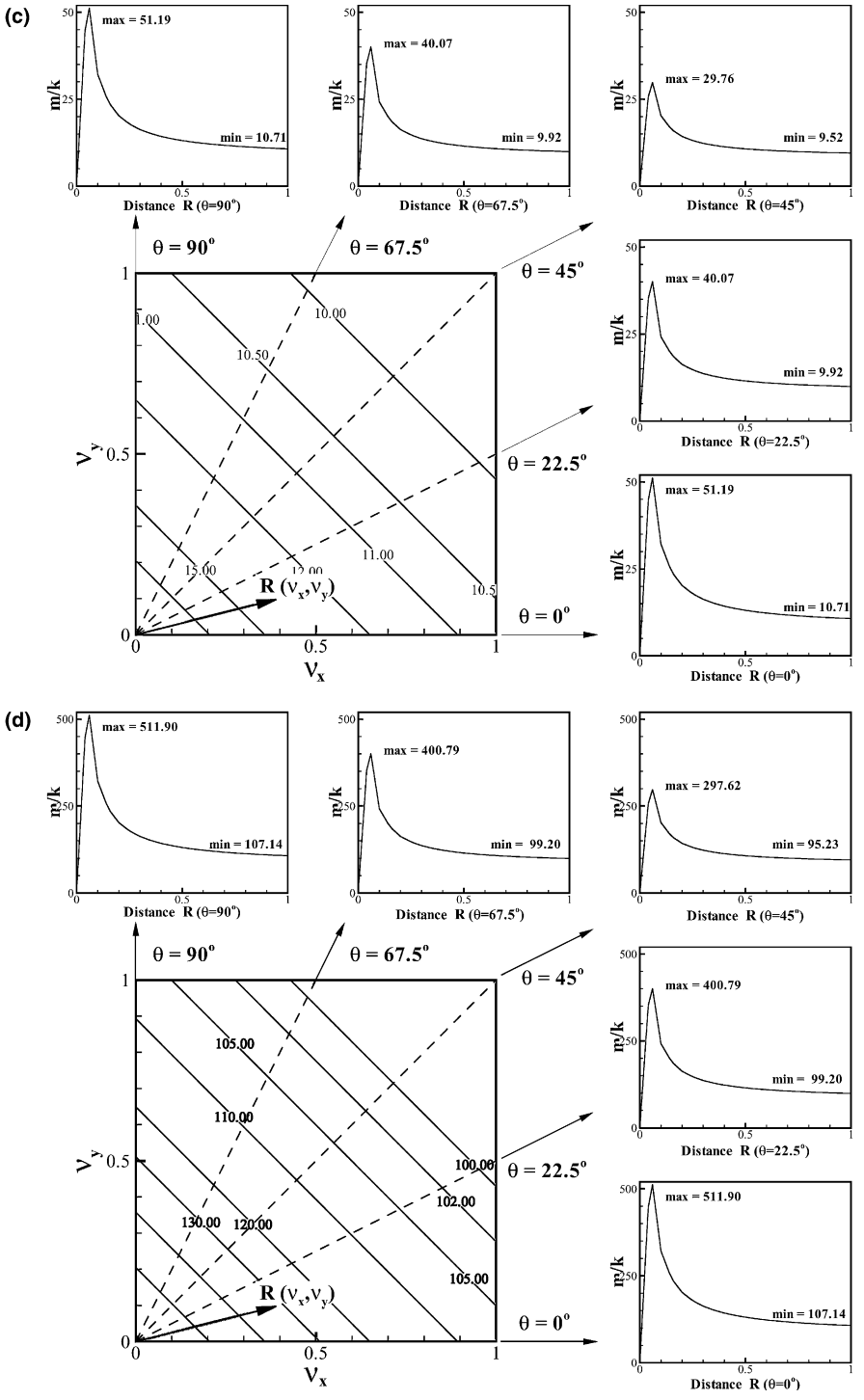

Fig. 4 (*continued*)

$$k_r = \frac{-\overline{p}}{\frac{v_x}{Pe_x} + \frac{v_x}{Pe_x} + \frac{1}{2}\left(\frac{v_x R_x + 12}{\gamma_1^2} + \frac{v_y R_y + 12}{\gamma_2^2}\right)}, \tag{5.12}$$

$$k_i = \frac{-\overline{q}}{v_x + v_y}, \tag{5.13}$$

where

$$\overline{p} = \ln\left\{\sqrt{X^2 + Y^2}\right\}, \tag{5.14}$$

$$\overline{q} = \tan^{-1}\left\{\frac{Y}{X}\right\}. \tag{5.15}$$

In the above, X and Y are derived as

$$X = \frac{\overline{a}\cdot S_1 - \overline{b}\cdot S_2}{\overline{a}^2 + \overline{b}^2}, \tag{5.16}$$

$$Y = \frac{\overline{b}\cdot S_1 + \overline{a}\cdot S_2}{\overline{a}^2 + \overline{b}^2}, \tag{5.17}$$

where

$$\overline{a} = \left(\overline{A}_1 + \overline{A}_9\right)\cos(\gamma_1 + \gamma_2) + \left(\overline{A}_2 + \overline{A}_8\right)\cos\gamma_2 + \left(\overline{A}_3 + \overline{A}_7\right)\cos(\gamma_1 - \gamma_2) + \left(\overline{A}_4 + \overline{A}_6\right)\cos\gamma_1 + \overline{A}5, \tag{5.18}$$

$$\overline{b} = \left(\overline{A}_1 - \overline{A}_9\right)\sin(\gamma_1 + \gamma_2) + \left(\overline{A}_2 - \overline{A}_8\right)\sin\gamma_2 + \left(\overline{A}_7 - \overline{A}_3\right)\sin(\gamma_1 - \gamma_2) + \left(\overline{A}_4 - \overline{A}_6\right)\sin\gamma_1, \tag{5.19}$$

$$S_1 = (6 - 3\ell_1)\left(e^{\frac{\overline{p}}{6}}\cos\frac{\overline{q}}{6} + e^{\frac{5\overline{p}}{6}}\cos\frac{5\overline{q}}{6}\right) + \ell_1 + 3\ell_2\left(e^{\frac{\overline{p}}{6}}\sin\frac{\overline{q}}{6} + e^{\frac{5\overline{p}}{6}}\sin\frac{5\overline{q}}{6}\right), \tag{5.20}$$

$$S_2 = (6 - 3\ell_1)\left(e^{\frac{\overline{p}}{6}}\sin\frac{q}{6} + e^{\frac{5\overline{p}}{6}}\sin\frac{5\overline{q}}{6}\right) - \ell_2 + 3\ell_2\left(e^{\frac{\overline{p}}{6}}\cos\frac{\overline{q}}{6} + e^{\frac{5\overline{p}}{6}}\cos\frac{5\overline{q}}{6}\right). \tag{5.21}$$

Coefficients ℓ_1 and ℓ_2 shown in (5.20) and (5.21) are detailed in Appendix A.

We plot k_r and k_i against (v_x, v_y) and (Pe_x, Pe_y) (fixed (R_x, R_y)) in Fig. 5. It is seen that k_i agrees perfectly with (γ_1, γ_2) in the small wavenumber range. The larger the wavenumber, the less satisfactory is the predicted phase. In contrast to k_i, the amplitude error is exhibited even in the small wavenumber range. In Fig. 6, we plot the ratio of the numerical group velocity $C_g(\equiv \frac{1}{2}(\frac{d\omega}{d\gamma_1} + \frac{d\omega}{d\gamma_2}))$ with respect to the analytical wave velocity, where $\omega(\equiv a\alpha\frac{k_i}{\gamma_1} + b\beta\frac{k_i}{\gamma_2})$ is obtained from the dispersion equation. In the shaded region (or phase-leading region), the value of $\frac{C_g}{C_e}$ is larger than 1. It is found that C_g always has a value smaller than the analytical propagation speed in the larger range of (γ_1, γ_2). The proposed scheme of the fourth-order temporal accuracy is, thus, phase-lagging or phase-leading, depending on the values of (γ_1, γ_2).

We also conduct Fourier (or von Neumann) stability analysis [13]. Let $\chi_x = \chi_y = \frac{2\pi m}{2L}h$ $(m = 0, 1, 2, \ldots, M)$, h be the grid size, and $2L$ be the period of fundamental frequency ($m = 1$), the amplification factor $G(\equiv \frac{\phi_{i,j}^{n+1}}{\phi_{i,j}^{n}})$ is derived as

$$G = e^{\overline{p}}(\cos\overline{q} + \mathbf{i}\sin\overline{q}). \tag{5.22}$$

As seen in Fig. 7(a), $|G|$ is always smaller than one. The proposed scheme is, thus, unconditionally stable. The amplification factor shown in (5.22) can be rewritten in its exponential form as $G = |G|\, e^{\mathbf{i}\theta}$, where θ is the phase angle

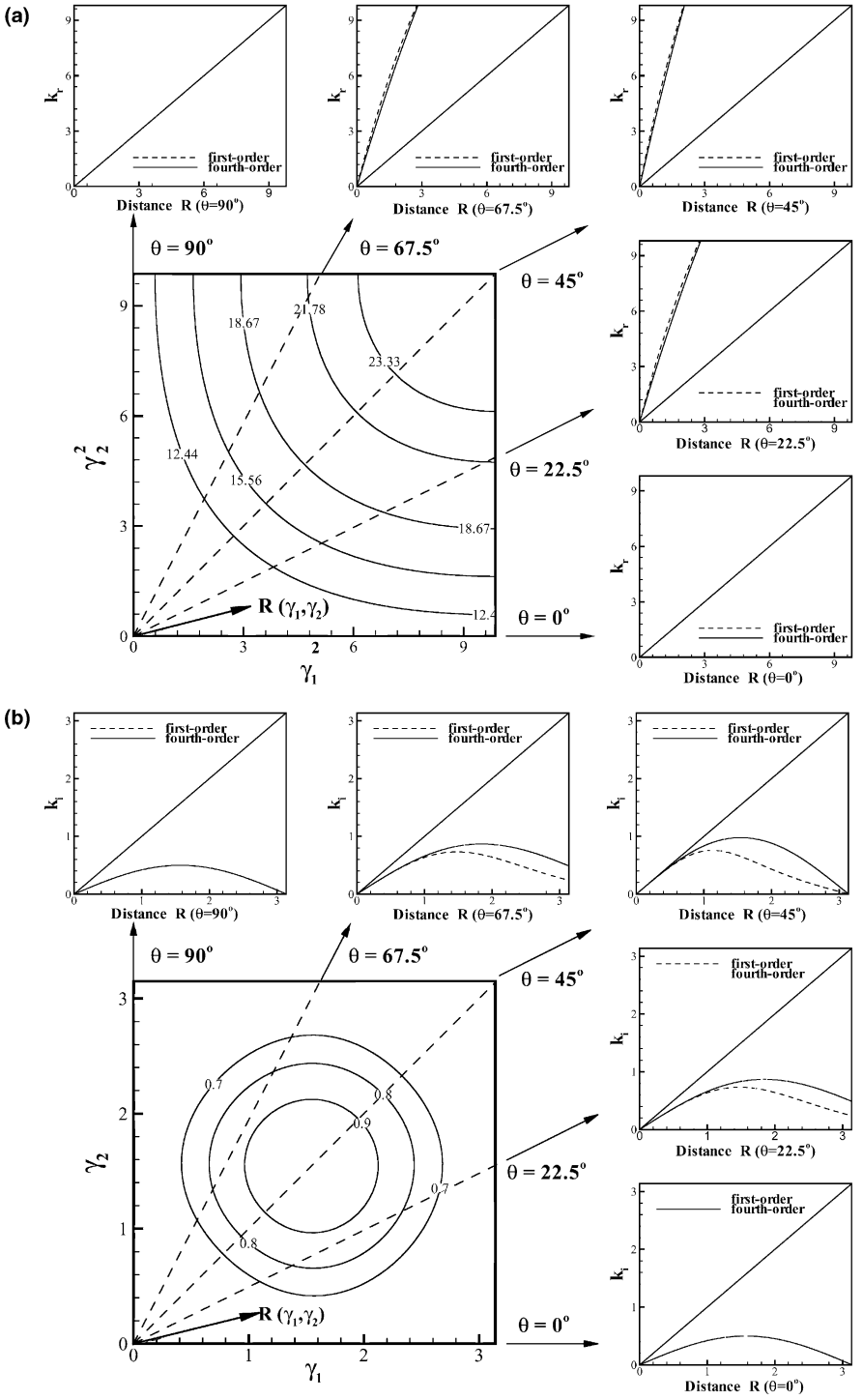

Fig. 5. Plots of k_r and k_i against (γ_1^2, γ_2^2) and (γ_1, γ_2), respectively, for the first-order and fourth-order temporal schemes (summarized in Table 1) at $Pe_x = Pe_y = 10^4$, $R_x = R_y = 0$ and $v_x = v_y = 0.1$ (a) k_r; (b) k_i.

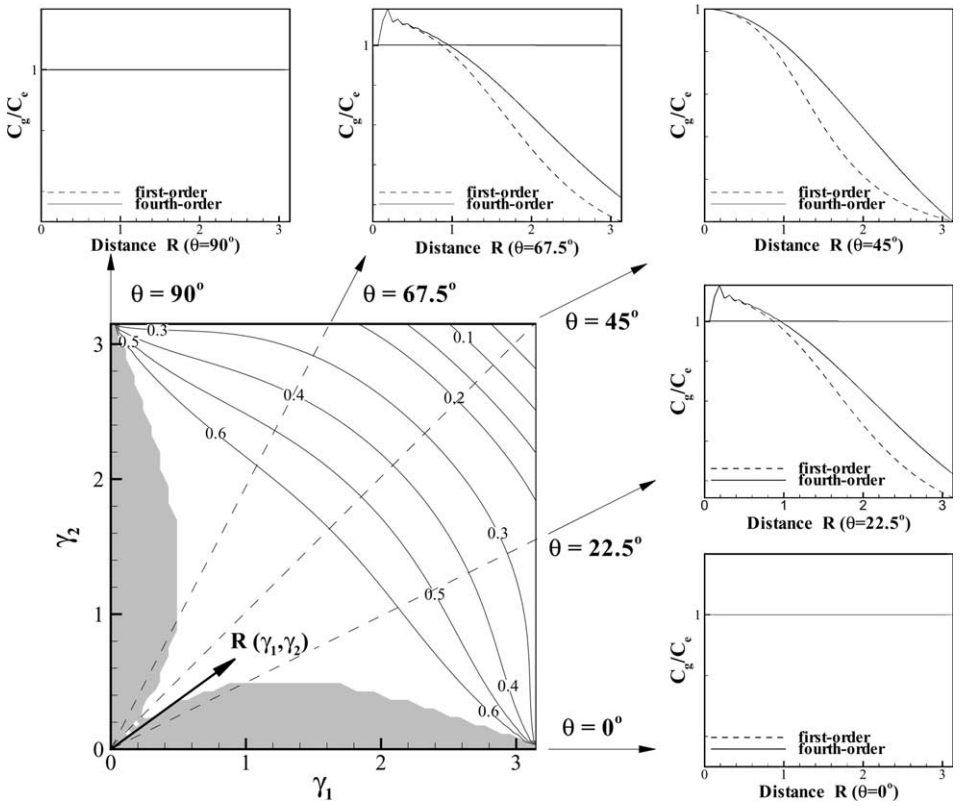

Fig. 6. Plots of the group velocity ratio $\frac{C_g}{C_e}$ against the modified wave-number (γ_1, γ_2) at $Pe_x = Pe_y = 10^4$, $R_x = R_y = 0$ and $v_x = v_y = 0.1$ for two temporal schemes (summarized in Table 1) of different accuracy orders. The shaded region denotes the phase-leading region.

$$\theta = \tan^{-1}\left|\frac{\mathrm{Im}(G)}{\mathrm{Re}(G)}\right|. \tag{5.23}$$

The exact phase angle θ_e can be derived as $-(\chi_x v_x + \chi_y v_y)$. Therefore, the relative phase shift error over an arbitrary time interval can be defined as

$$\frac{\theta}{\theta_e} = \frac{\tan^{-1}\left|\frac{\mathrm{Im}(G)}{\mathrm{Re}(G)}\right|}{-(\chi_x v_x + \chi_y v_y)}. \tag{5.24}$$

We plot $\frac{\theta}{\theta_e}$ against (χ_x, χ_y), (v_x, v_y), (Pe_x, Pe_y), and (R_x, R_y) in Fig. 7(b).

Finally, we will demonstrate that the proposed implicit DRP finite difference scheme can conditionally resolve sharp solution profile. Under the circumstances that $a_{ij} \leqslant 0$ with $i \neq j$ and $|a_{ii}| \geqslant \sum |a_{ij}| (i \leqslant j)$, the banded matrix $\underline{\underline{\mathbf{A}}}$ shown in Eq. (4.29) or (5.3) is, by definition, irreducible diagonally dominant. The matrix of this type is called an M-matrix. Monotone solutions can be computed from the M-matrix equation due to the inherent property $\underline{\underline{\mathbf{A}}}^{-1} > 0$. By following the M-matrix theory [14], we plot in Fig. 8 the M-matrix regions. It is seen that the shaded monotone region changes very litter with the Courant number as the Peclet number becomes larger than 10. The proposed conditionally monotonic scheme can, as a result, resolve any possible sharp gradient as v_x and v_y become smaller than 0.23. For the

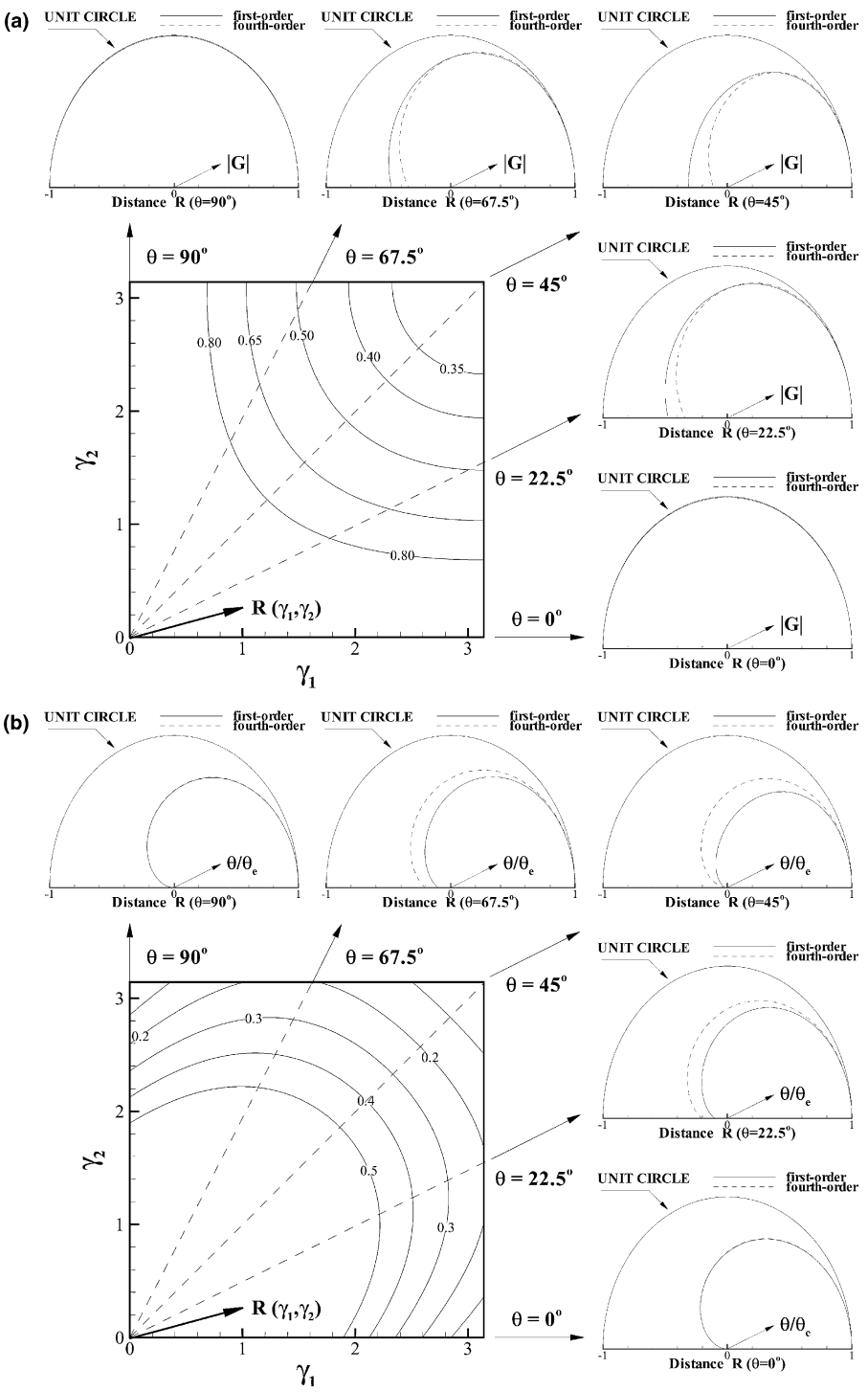

Fig. 7. Plots of $|G|$ and $\frac{\theta}{\theta_e}$ against (γ_1, γ_2) at $Pe_x = Pe_y = 10^4$, $R_x = R_y = 0$ and $v_x = v_y = 0.1$ for two temporal schemes summarized in Table 1. (a) Amplification factor $|G|$; (b) phase angle ratio $\frac{\theta}{\theta_e}$.

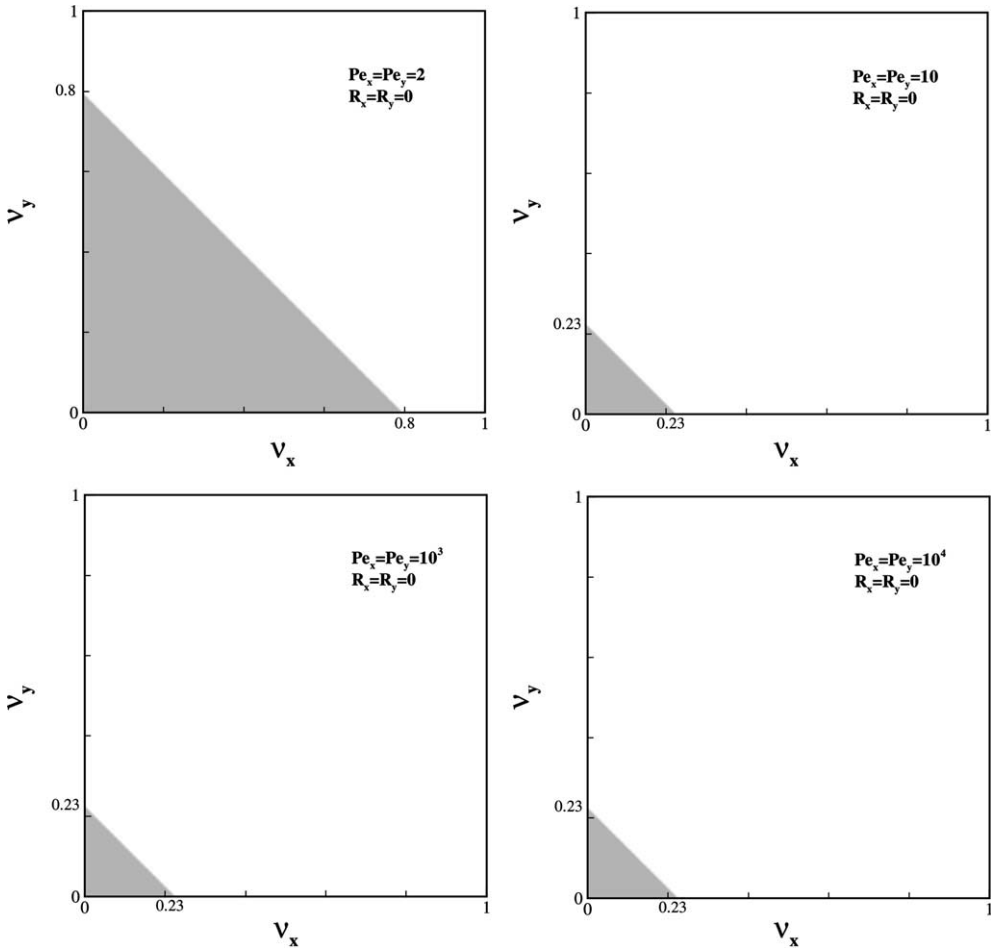

Fig. 8. In the shaded regions, the matrix equations are classified as being monotonic at $R_x = R_y = 0$. (a) $Pe_x = Pe_y = 2$; (b) $Pe_x = Pe_y = 10$; (c) $Pe_x = Pe_y = 10^3$; (d) $Pe_x = Pe_y = 10^4$.

Table 1
Comparison of the first- and fourth-order temporal schemes $A_{ij}\phi_{ij}^{n+1} - \overline{F}_{ij}^{n+1} = B_{ij}$

	First-order	Fourth-order	Equation no.
A_{ij}	1	12	(5.1)
B_{ij}	ϕ_{ij}^{n}	$6(\phi_{ij}^{n+\frac{1}{6}} + \phi_{ij}^{n+\frac{5}{6}}) - \overline{F}_{ij}^{n} + 3(\overline{F}_{ij}^{n+\frac{1}{6}} + \overline{F}_{ij}^{n+\frac{5}{6}})$	(5.1)
k_r	$\frac{-\overline{p}}{\frac{v_x}{Pe_x}+\frac{v_y}{Pe_y}+\frac{1}{2}(\frac{R_x v_x+1}{\gamma_1^2}+\frac{R_y v_y+1}{\gamma_2^2})}$	$\frac{-\overline{p}}{\frac{v_x}{Pe_x}+\frac{v_y}{Pe_y}+\frac{1}{2}(\frac{R_x v_x+12}{\gamma_1^2}+\frac{R_y v_y+12}{\gamma_2^2})}$	(5.12)
k_i	$\frac{-\overline{q}}{v_x+v_y}$	$\frac{-\overline{q}}{v_x+v_y}$	(5.13)
$\overline{p}$	$\ln\{\frac{1}{\overline{a}\cos\overline{q}+\overline{b}\sin\overline{q}}\}$	$\ln\{\sqrt{X^2+Y^2}\}$	(5.14)
$\overline{q}$	$\tan^{-1}\{\frac{\overline{b}}{\overline{a}}\}$	$\tan^{-1}\{\frac{Y}{X}\}$	(5.15)
X	0	$\frac{\overline{a}\cdot S_1-\overline{b}\cdot S_2}{\overline{a}^2+\overline{b}^2}$	(5.16)
Y	0	$\frac{\overline{b}\cdot S_1+\overline{a}\cdot S_2}{\overline{a}^2+\overline{b}^2}$	(5.17)

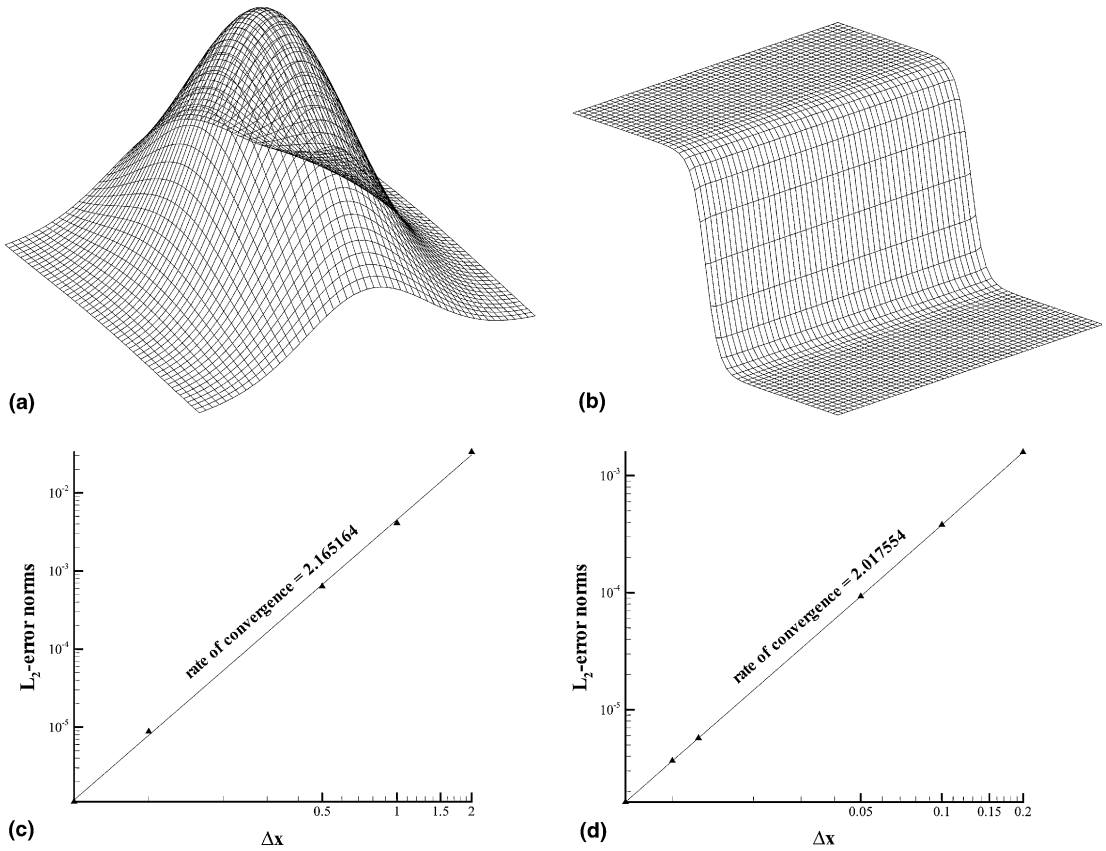

Fig. 9. The simulated solutions for the two problems considered in Section 6.1: (a) the Gaussian solution profile; (b) the hyperbolic tangent solution profile; (c) the rate of convergence for the problem given in (6.1); (d) the rate of convergence for the problem given in (6.2).

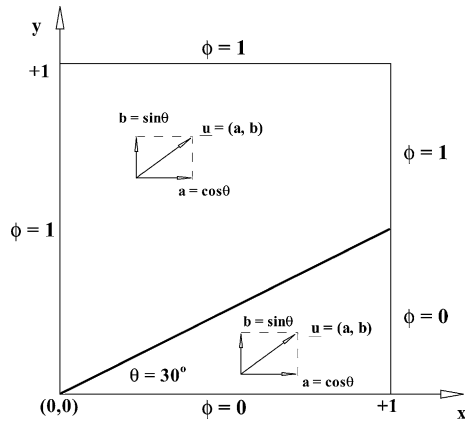

Fig. 10. Schematic of the advection–diffusion problem considered in Section 6.2.

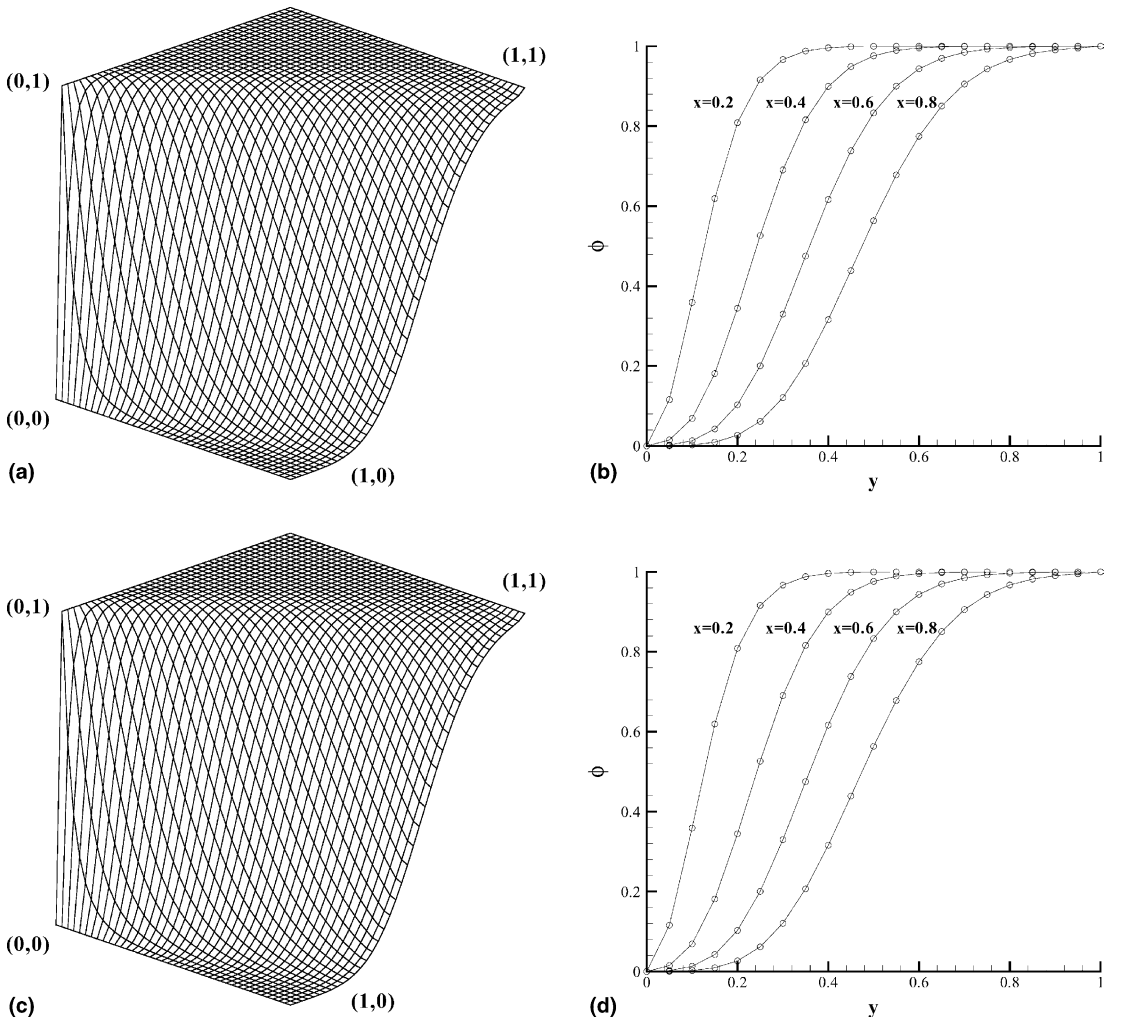

Fig. 11. The simulated solutions for ϕ and their sectional profiles at $x = \frac{1}{5}, \frac{2}{5}, \frac{3}{5}, \frac{4}{5}$. (a) and (b) $k = 10^{-1}$; (c) and (d) $k = 10^{-3}$.

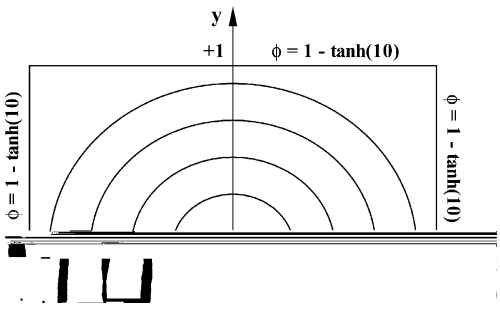

Fig. 12. Schematic of the Smith–Hutton problem considered in Section 6.3.

comparison of the currently proposed fourth-order temporal scheme with the conventional first-order temporal scheme used in the results, we summarized two schemes in expressions as well as in scheme nature in Table 1 for completeness.

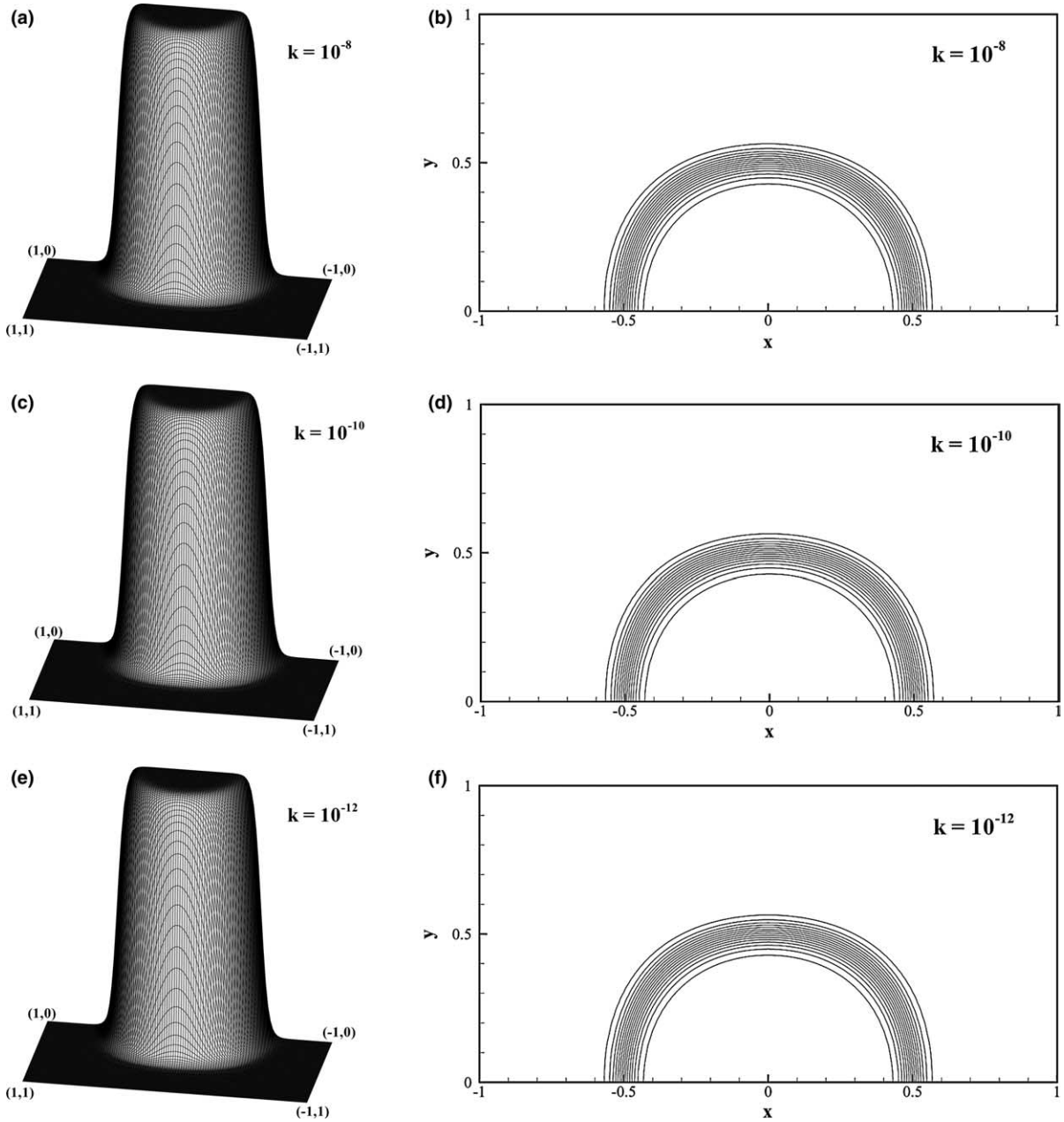

Fig. 13. The simulated ϕ at different k for the problem considered in Section 6.3 using the monotone DRP finite-difference model. (a) and (b) $k = 10^{-8}$; (c) and (d) $k = 10^{-10}$; (e) and (f) $k = 10^{-12}$.

6. Numerical studies

6.1. Gaussian and hyperbolic tangent problem

The model equation (4.26) in $[0,1]\times[0,1]$ is solved at the given values of $(a,b) = (1,0)$, $k = 10^{-10}$ and $c = 0$. Two different source terms f are specified to render their respective exact solutions given below [15]:

$$\phi(x,y) = \exp\left(-\frac{(x-0.5)^2}{0.2} - \frac{3(y-0.5)^2}{0.2}\right), \tag{6.1}$$

$$\phi(x,y) = \frac{1}{2}\left(1 - \tanh\left(\frac{x-0.5}{0.05}\right)\right). \tag{6.2}$$

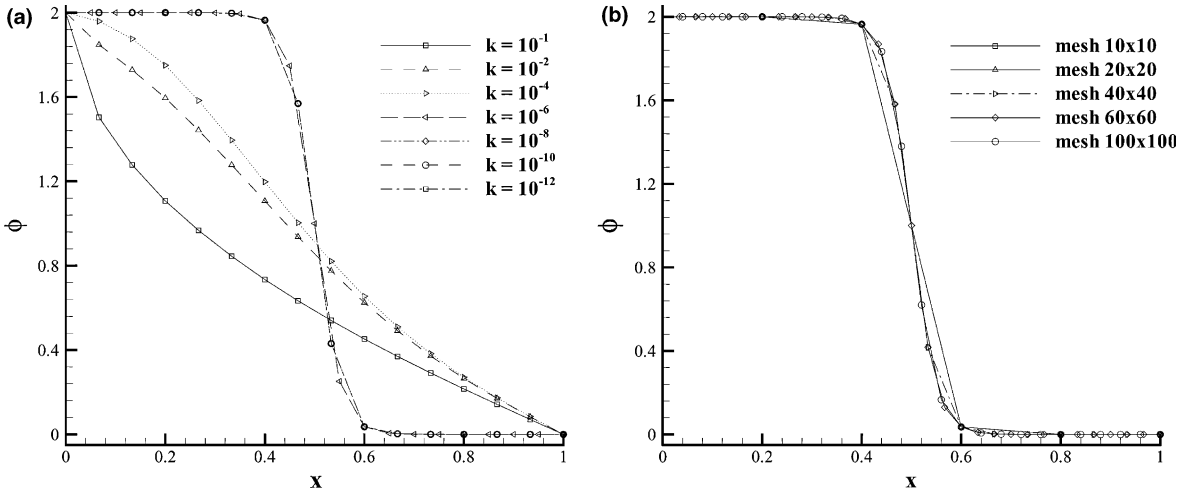

Fig. 14. The simulated ϕ at $y = 0$ against x ($0 \leqslant x \leqslant 1$). (a) Solutions obtained at different k; (b) solutions obtained at $k = 10^{-12}$ and different mesh resolutions.

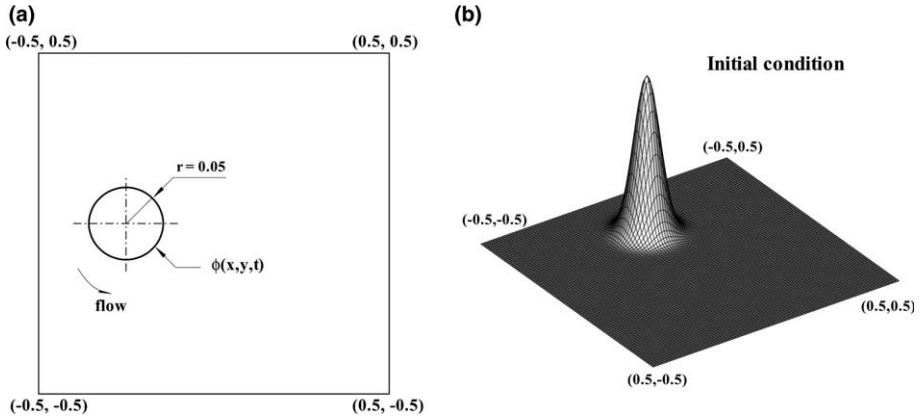

Fig. 15. (a) Schematic of the solid-body rotation test problem; (b) three-dimensional illustration of the prescribed initial scalar field.

Simulations were carried out at $\Delta x = \Delta y = \frac{1}{10}, \frac{1}{20}, \frac{1}{40}, \frac{1}{80}$ and $\frac{1}{160}$ to obtain the finite difference errors cast in L_2-norm form. This is followed by plotting in Fig. 9 the value of $\log(\frac{err_1}{err_2})$ against $\log(\frac{h_1}{h_2})$, where err_1 and err_2 error norms are obtained at consecutively refined mesh sizes h_1 and h_2, to obtain the scheme's spatial rate of convergence. Good agreement with the exact solutions and the rapid convergences are both demonstrated in the two simulated solutions.

6.2. Skew convection–diffusion problem

The problem schematic in Fig. 10 has been a good scenario for validating the upwinding method [16]. The cavity of unit length is divided into two by the line, which passes through $(0,0)$ with a slope of

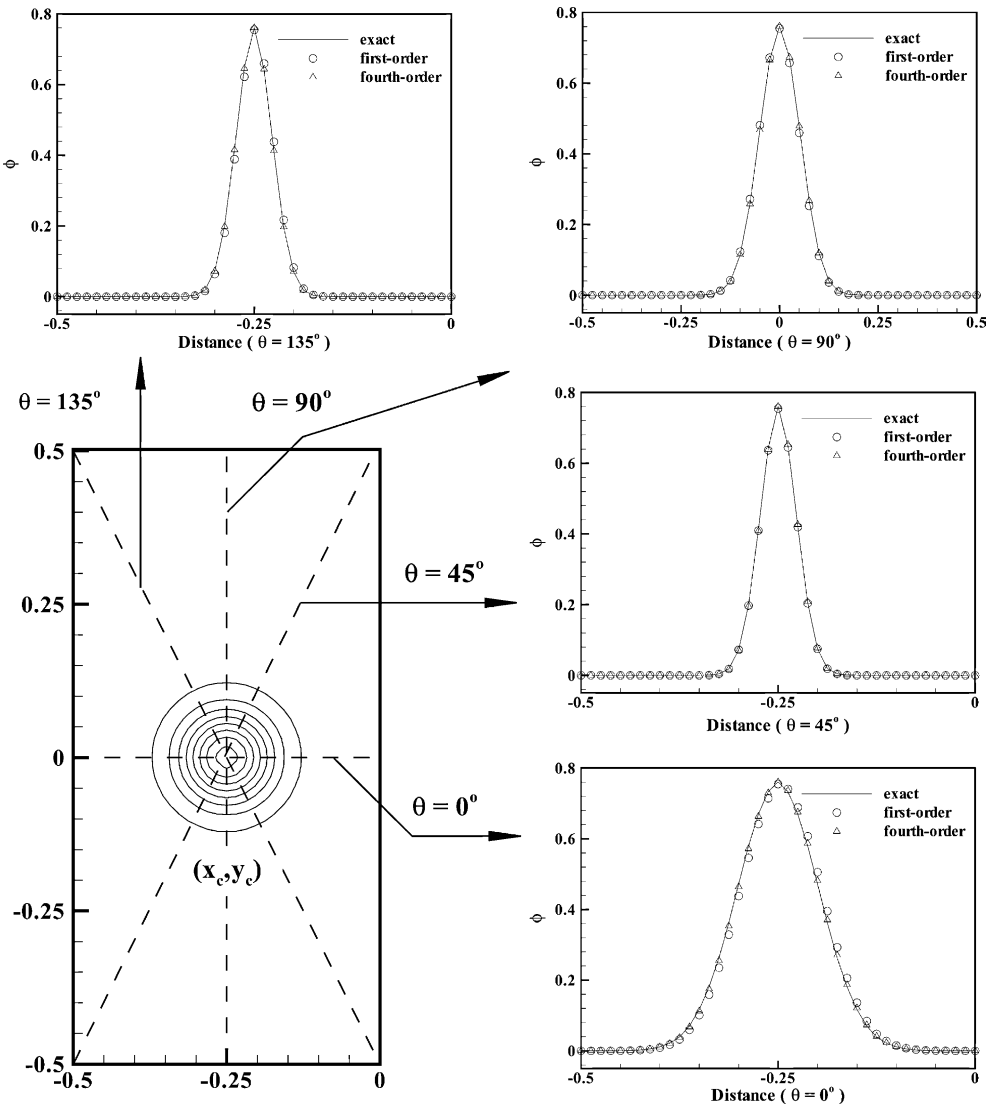

Fig. 16. The simulated solution profiles for the problem considered in Section 6.4.

$\tan^{-1}(b/a)$. The unit velocity vector (a,b) parallel to the dividing line is considered in a 40×40 uniformly discretized mesh system for fluids with two different diffusivities $k = 10^{-1}$ and 10^{-3}. Subject to the boundary condition schematic in Fig. 10 for the working variable, a shear layer is seen in the vicinity of the dividing line. As Fig. 11 shows, non-oscillatory solutions are seen to be well predicted in regions near and away from the dividing line.

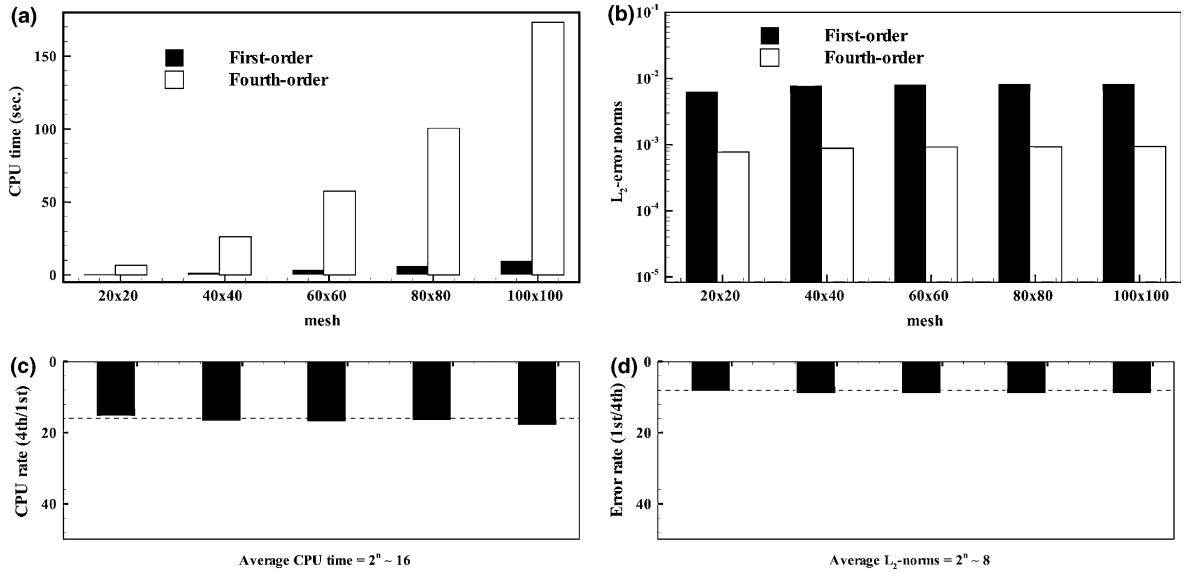

Fig. 17. The simulated CPU times and L_2-error norms for the problem considered in Section 6.4. (a) The CPU times; (b) the L_2-error norms.

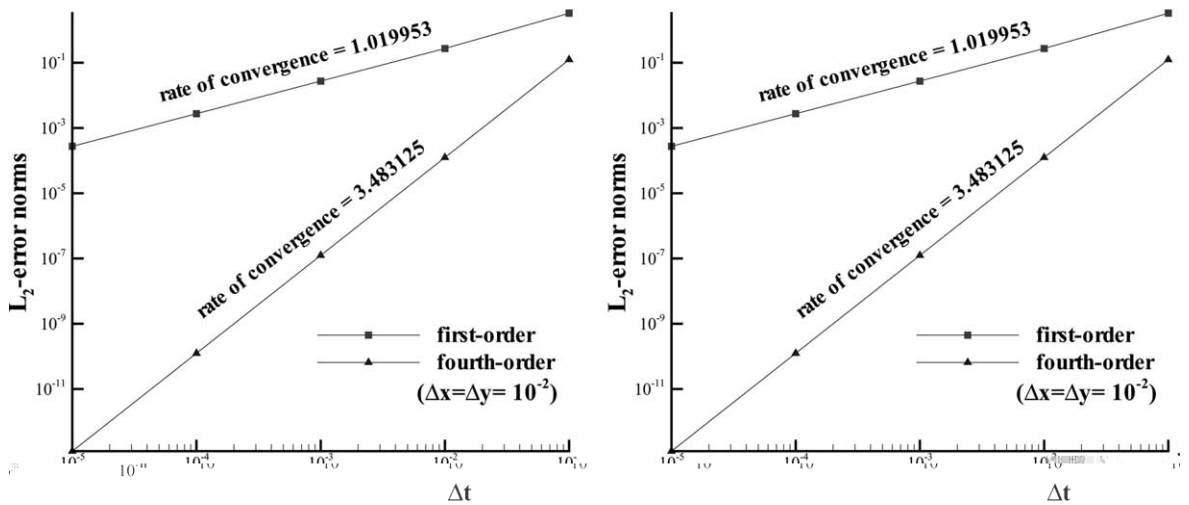

Fig. 18. The simulated rates of convergence for the problem considered in Section 6.4. (a) The temporal rates of convergence; (b) the spatial rates of convergence.

6.3. Convection–diffusion problem of Smith and Hutton

The problem of Smith and Hutton [17] is investigated at $a = 2y(1 - x^2)$ and $b = -2x(1 - y^2)$. Along the inlet schematic in Fig. 12, the working variable ϕ is prescribed as follows:

$$\phi(-1 \leqslant x \leqslant 0, y = 0) = 1 + \tanh(10(2x + 1)). \tag{6.3}$$

Along $x = -1$, $y = 1$ and $x = 1$, we prescribe $\phi = 1 - \tanh(10)$ while at the outlet ($0 \leqslant x \leqslant 1, y = 0$) we specify a zero gradient condition for ϕ. For the case with $\Delta x = \Delta y = 10^{-2}$, the DRP solutions are obtained at $k = 10^{-12}$, 10^{-10}, 10^{-8}, 10^{-6}, 10^{-4} and 10^{-2}. As Fig. 13 reveals, the efficacy of the proposed finite difference scheme is clearly demonstrated. We summarize the effects of Peclet number and grid size in Fig. 14 based on the simulated solutions at the exit boundary.

6.4. Rotation of a cone-shaped scalar field

We will then consider the transient problem, schematic in Fig. 15, with the following initial condition:

$$\phi(x, y, t = 0) = \exp\left[-\frac{(\bar{x} - x_c)^2 + (\bar{y} - y_c)^2}{2M^2}\right]. \tag{6.4}$$

In $-0.5 \leqslant x, y \leqslant 0.5$, the model equation investigated at $(a, b) = (-4y, 4x)$ is amenable to the exact solution given by

$$\phi(x, y, t) = \frac{2M^2}{2M^2 + 4Dt} \exp\left[-\frac{(\bar{x} - x_c)^2 + (\bar{y} - y_c)^2}{2M^2 + 4Dt}\right], \tag{6.5}$$

where $(\bar{x}, \bar{y}) = (x\cos 4t + y\sin 4t, -x\sin 4t + y\cos 4t)$, $M^2 = 2 \times 10^{-3}$, $k = D = 10^{-4}$ and $(x_c, y_c) = (-0.25, 0)$. Solutions computed at $\Delta t(=10^{-3})$, $\Delta x = \Delta y(=10^{-2})$ are plotted in Fig. 16. It is clearly seen from the time-evolving contours at $t = \frac{\pi}{8}, \frac{\pi}{4}, \frac{\pi}{2}, \pi$ that solution symmetry can be well retained irrespective of the specified

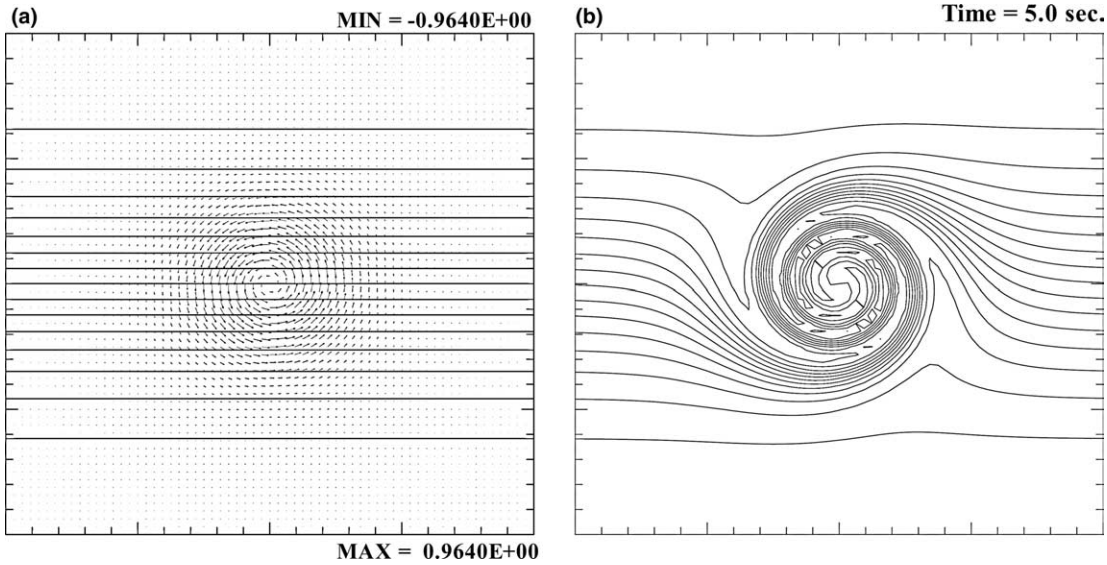

Fig. 19. (a) Initial solution considered for the mixing of two fluid flows of different temperatures; (b) exact solution.

rotating velocity field. As before, calculations were performed to obtain the L_2-error norms at uniform grid sizes and time increments.

For the sake of assessing two temporal schemes (tabulated in Table 1), we plot in Fig. 17 the needed CPU times and L_2-error norms against different mesh sizes. As seen from these simulated results, the increase in prediction accuracy with a factor of 8 for the fourth-order accurate scheme is accompanied with the increased CPU time with a factor of 16 ($\approx 2^4$). The spatial and temporal rates of convergence for the solution $\phi(t = \pi, x, y)$ computed at $\Delta t = 10^{-3}$ and $\Delta x = \Delta y = 10^{-2}$ are also plotted in Fig. 18.

6.5. Mixing of hot and cold fronts

We also consider the mixing of cold and warm fluids in $-4 \leqslant x, y \leqslant 4$. Initially, the temperature $\phi(x, y, t)$ schematic in Fig. 19(a) is given by

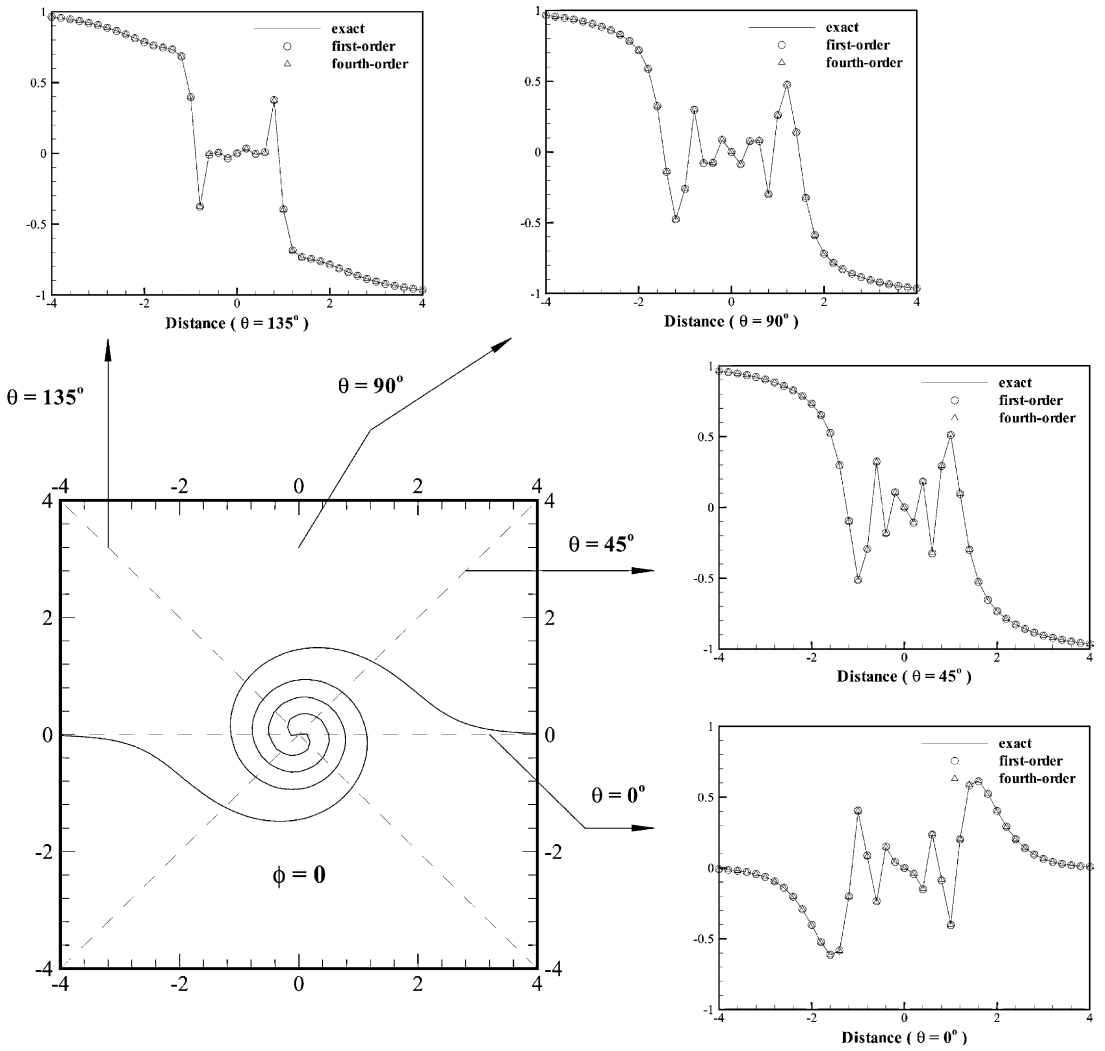

Fig. 20. The simulated ϕ for the mixing of hot and cold fluids considered in Section 6.5.

$$\phi(x, y, t = 0) = -\tanh\left(\frac{y}{2}\right). \tag{6.6}$$

The flow under investigation is centered at the origin $(-\overline{T}\frac{y}{r}, \overline{T}\frac{x}{r})$, where $\overline{T}\left(\equiv \frac{\mathrm{sech}^2(r)\tanh(r)}{\max[\mathrm{sech}^2(r)\tanh(r)]}\right)$ denotes the ratio of the tangential velocity at a location that is distant from $(0, 0)$ with a length of r. For the sake of comparison, we plot in Fig. 19(b) the exact solution at the limiting case ($k = 0$) [18]:

$$\phi(x, y, t) = -\tanh\left[\frac{y}{2}\cos\omega t - \frac{x}{2}\sin\omega t\right]. \tag{6.7}$$

In the above, $\omega = \frac{\overline{T}}{r}$ denotes the rotation frequency.

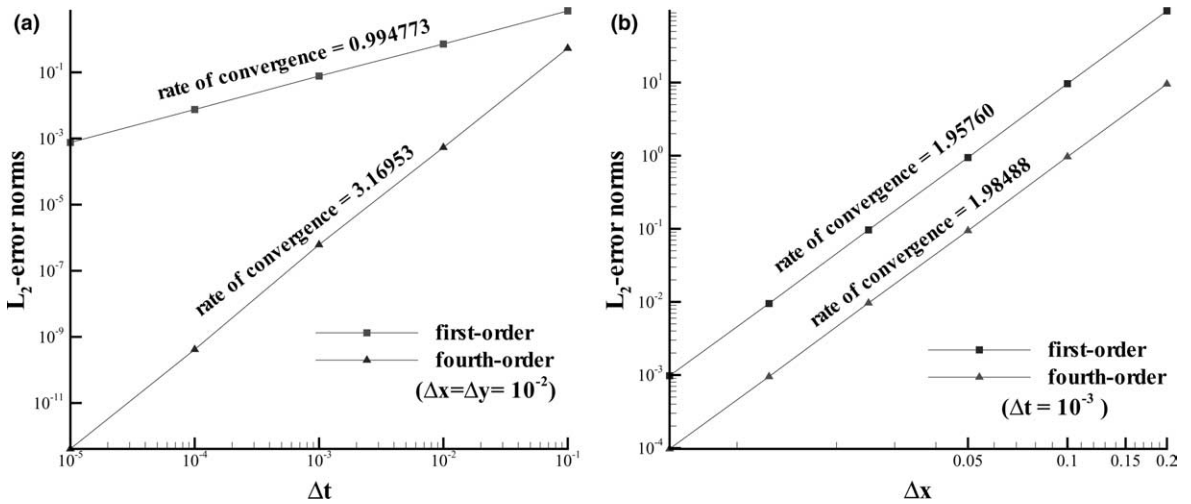

Fig. 21. The simulated rates of convergence for the problem considered in Section 6.5. (a) The temporal rates of convergence; (b) the spatial rates of convergence.

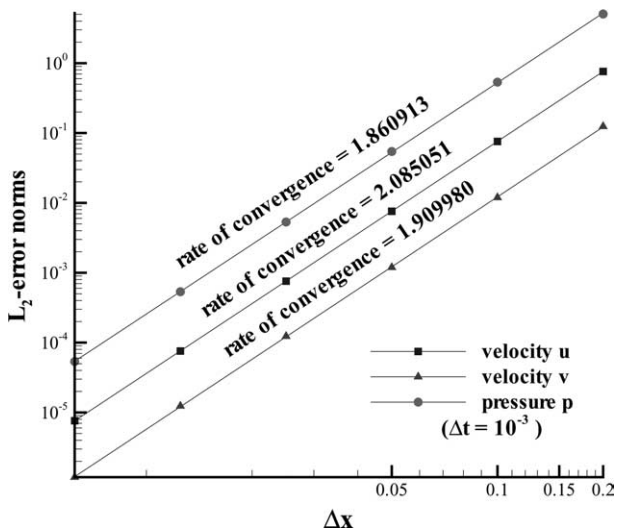

Fig. 22. The simulated rates of convergence for the Navier–Stokes problem with the exact solutions given in Eqs. (6.8)–(6.10).

Fig. 20 shows the solution $\phi(x, y, t = 5.0)$ obtained at $c = 0$, $k = 0$ and $\Delta x = \Delta y = 10^{-2}$. In the rotating velocity field, the simulated temperature is seen to take a spiral form and change sharply near the interface of warm and cold fluids. The spatial and temporal rates of convergence for the solution computed at $t = 5$ are also plotted in Fig. 21 under the conditions of $\Delta t = 10^{-3}$ and $\Delta x = \Delta y = 10^{-2}$.

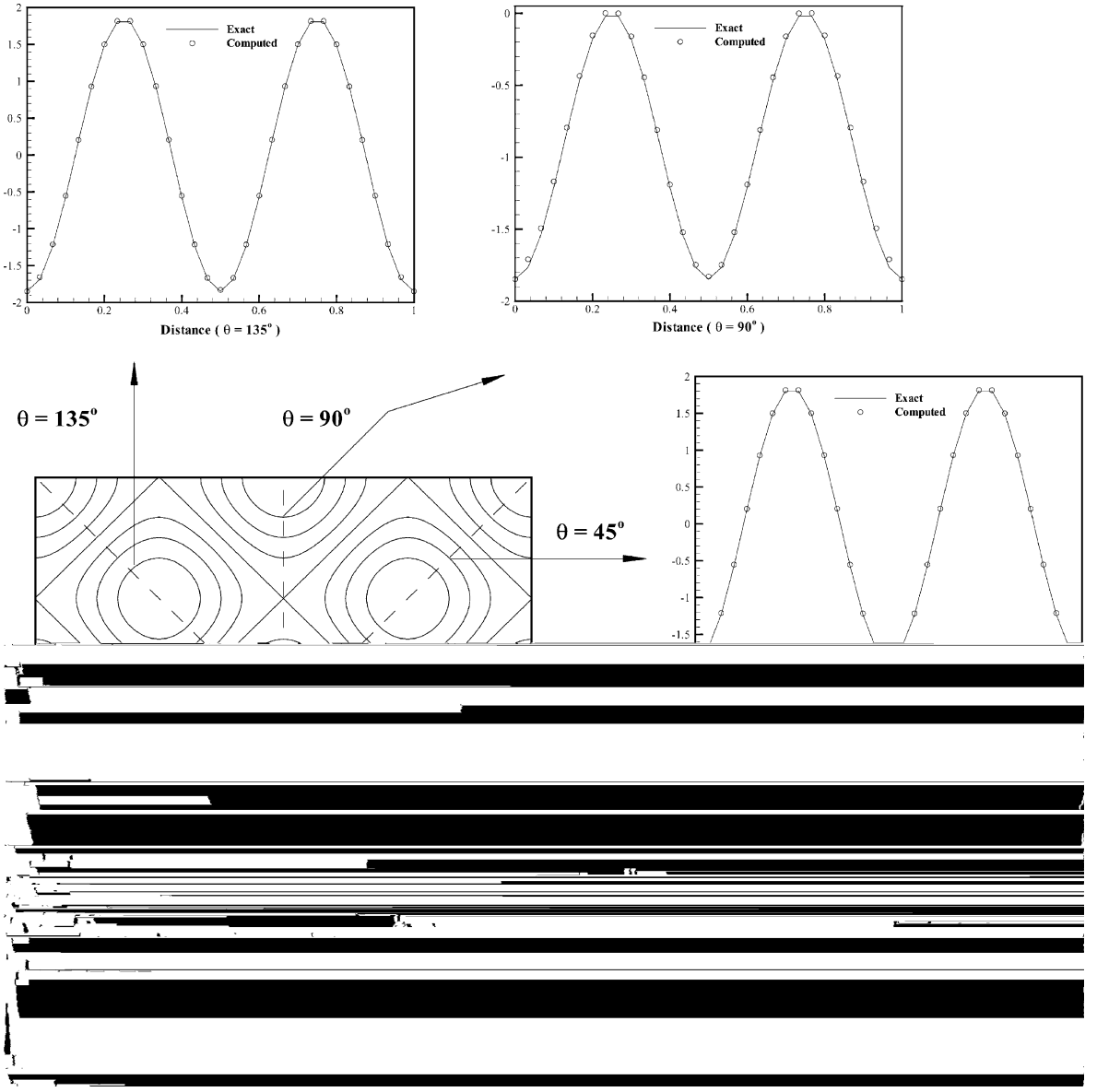

Fig. 23. The simulated pressure contours and distributions for the unsteady problem considered in Section 6.6.

6.6. Validation of the proposed Navier–Stokes method

Encouraged by the success of solving the scalar transport equation using the proposed scheme, the transient Navier–Stokes equations are solved in a square ($0 \leqslant x, y \leqslant 1$) for the problem amenable to the following exact solution:

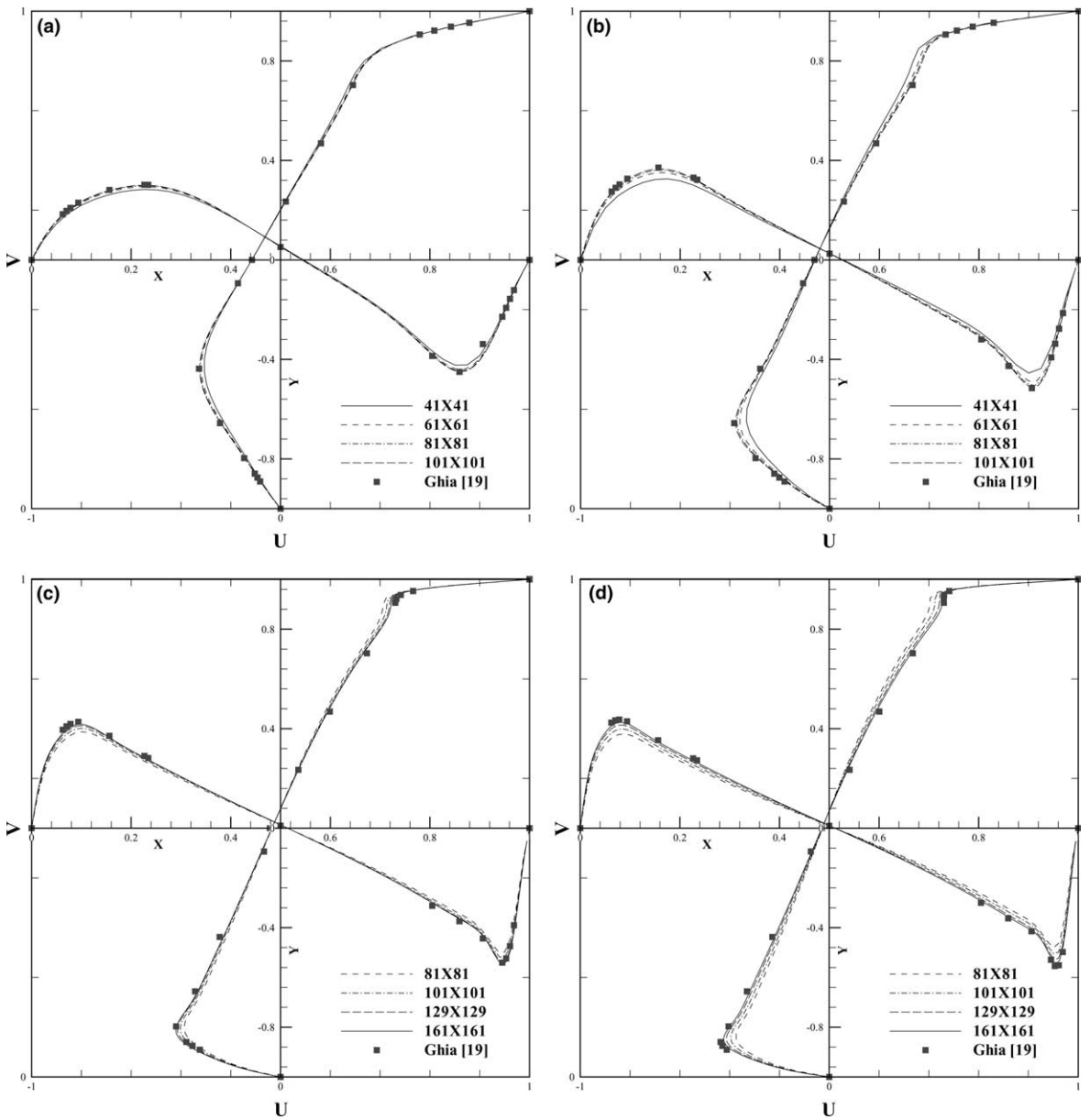

Fig. 24. Comparison of the simulated and Ghia's velocity profiles for $u(x, 0.5)$ and $v(0.5, y)$. (a) $Re = 400$; (b) $Re = 1000$; (c) $Re = 3200$ (d) $Re = 5000$.

$$u = 1 + 2\cos[2\pi(x-t)]\sin[2\pi(y-t)]\exp\left(\frac{-8\pi^2}{Re}t\right), \tag{6.8}$$

$$v = 1 - 2\sin[2\pi(x-t)]\cos[2\pi(y-t)]\exp\left(\frac{-8\pi^2}{Re}t\right), \tag{6.9}$$

$$p = c_1 - \{\cos[4\pi(x-t)] + \cos[4\pi(y-t)]\}\exp\left(\frac{-16\pi^2}{Re}t\right). \tag{6.10}$$

In Fig. 22, we plot the computed rates of convergence for **u** and p according to

$$C = \frac{\log(E_2/E_1)}{\log(h_2/h_1)}, \tag{6.11}$$

where E is the error measured in its discrete L_2-norm form

$$E = \left[\sum_{i=1}^{N}\left(\phi_{ij} - \Phi_{ij}\right)^2 \Delta x_i \Delta y_j\right]^{1/2}. \tag{6.12}$$

In the above, $\phi_{i,j} = \phi(x_i, y_j)$ denotes the finite difference solution at (i,j) and Φ_{ij} is the corresponding exact solution in $0 \leqslant x, y \leqslant 1$. In Fig. 23, we plot the simulated contours for **u** and p at $t = \pi$, $Re = 10^4$, $\Delta x = \Delta y = \frac{1}{64}$ and $\Delta t = 10^{-3}$. Computations are also performed at four mesh sizes $h = \frac{1}{2^n}$, where $n = 4, 5, 6, 7$ at $Re = 10^4$ and $\Delta t = 10^{-3}$ for the sake of completeness. In view of the L_2-norm errors plotted in Fig. 22, the proposed method is validated.

6.7. Lid-driven cavity flow problem

With L as the characteristic length, U the characteristic velocity, the Reynolds number $Re(\equiv UL/\mu)$ for the lid-driven fluid flow with viscosity μ is 5000. We continuously refine the mesh in the square cavity and plot the grid-independent velocity profiles $u(0.5, y)$ and $v(x, 0.5)$ in Fig. 24. Since the agreement between

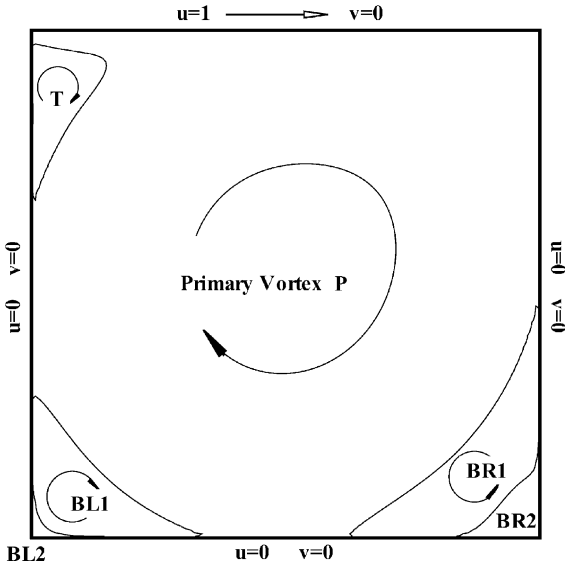

Fig. 25. Schematic of the eddy centers in the lid-driven cavity.

Table 2
The simulated four eddy centers (primary eddy P, corner eddies BL and BR and the eddy T near the cavity roof) for the cases with $Re = 400$, 1000, 3200 and 5000

Symbol	Authors	*Re*			
		400	1000	3200	5000
Primary	Present	0.5579, 0.6112	0.5331, 0.5745	0.5235, 0.5357	0.5207, 0.5305
	Ghia [19]	0.5547, 0.6055	0.5313, 0.5625	0.5165, 0.5469	0.5117, 0.5352
First	Present	–	–	0.0561, 0.8951	0.0622, 0.8986
T	Ghia [19]	–	–	0.0547, 0.8984	0.0625, 0.9102
BL	Present	0.0548, 0.0438	0.0821, 0.0754	0.0835, 0.1097	0.0747, 0.1272
	Ghia [19]	0.0508, 0.0469	0.0859, 0.0781	0.0859, 0.1094	0.0703, 0.1367
BR	Present	0.8807, 0.1261	0.8542, 0.1187	0.9051, 0.0650	0.8048, 0.0726
	Ghia [19]	0.8906, 0.1250	0.8594, 0.1094	0.8125, 0.0859	0.8086, 0.0742
Second	Present	0.0036, 0.0037	–	0.0075, 0.0076	0.0107, 0.0076
BL	Ghia [19]	0.0039, 0.0039	–	0.0078, 0.0078	0.0117, 0.0078
BR	Present	0.9897, 0.0076	0.9897, 0.0076	0.9812, 0.0076	0.9795, 0.0189
	Ghia [19]	0.9922, 0.0078	0.9922, 0.0078	0.9844, 0.0078	0.9805, 0.0195
Mesh points	Present	81	101	101	129
	Ghia [19]	257	129	129	257

the simulated and benchmark solutions of Ghia et al. [19] is extremely good, the applicability of employing the proposed scheme to simulate the high Reynolds number flow is confirmed. For the sake of completeness, the centers of three eddies at T, BL and BR schematic in Fig. 25 are summarized in Table 2 for $Re = 400$, 1000, 3200 and 5000. Good agreement with the comparison data [19] is also clearly revealed.

7. Concluding remarks

The present study employs the scheme of fourth-order temporal accuracy to solve the unsteady convection–diffusion transport equation. Employing Pade's approximation results in two explicit and two implicit spatial differential equations. For improving the convective stability, the two-dimensional dispersion-relation-preserving finite difference scheme is rigorously developed. For increasing the solution accuracy, a nodally exact artificial viscosity is introduced into the two-dimensional formulation. Dispersive and dissipative natures of the developed model have been extensively studied. Conditions that can result in the monotonic matrix equation for the investigated unsteady convection–diffusion equation are also derived. To validate the proposed scheme, we have considered problems amenable to exact solutions. The computed L_2-error norms and their resulting rates of convergence demonstrate the advantage of using the proposed scheme to solve for problems having smooth as well as sharply varying solution profiles. Fluid flows in a lid-driven cavity are also studied at different Reynolds numbers and the computed DRP solutions are shown to have good agreement with the benchmark solutions.

Acknowledgment

The financial support provided by the National Science Council under Grant NSC 92-2611-E-002-008 is gratefully acknowledged.

Appendix A

Coefficients ℓ_1 and ℓ_2 shown in (5.20) and (5.21) are expressed below in terms of $\overline{B}_i$ $(i = 1, 2, \ldots, 9)$:

$$\ell_1 = \left(\overline{B}_1 + \overline{B}_9\right)\cos(\gamma_1 + \gamma_2) + \left(\overline{B}_2 + \overline{B}_8\right)\cos\gamma_2 + \left(\overline{B}_3 + \overline{B}_7\right)\cos(\gamma_1 - \gamma_2) + \left(\overline{B}_4 + \overline{B}_6\right)\cos\gamma_1 + \overline{B}5, \tag{A.1}$$

$$\ell_2 = \left(\overline{B}_1 - \overline{B}_9\right)\sin(\gamma_1 + \gamma_2) + \left(\overline{B}_2 - \overline{B}_8\right)\sin\gamma_2 + \left(\overline{B}_7 - \overline{B}_3\right)\sin(\gamma_1 - \gamma_2) + \left(\overline{B}_4 - \overline{B}_6\right)\sin\gamma_1. \tag{A.2}$$

In the above, the coefficients $\overline{B}_i$ $(i = 1, 2, \ldots, 9)$ are

$$\overline{B}_i = \left(a_i v_x + b_i v_y\right) - \frac{1}{2}\left(\frac{v_x}{Pe_x} + \frac{v_y}{Pe_y}\right) + \frac{v_x R_x + v_y R_y}{56}, \quad i = 1, 3, 7, 9, \tag{A.3}$$

$$\overline{B}_j = \left(a_j v_x + b_j v_y\right) - 2\left(\frac{v_x}{Pe_x} + \frac{v_y}{Pe_y}\right) + \frac{v_x R_x + v_y R_y}{28}, \quad j = 2, 4, 6, 8, \tag{A.4}$$

$$\overline{B}_5 = \left(a_5 v_x + b_5 v_y\right) + 10\left(\frac{v_x}{Pe_x} + \frac{v_y}{Pe_y}\right) + \frac{2(v_x R_x + v_y R_y)}{7}, \tag{A.5}$$

where $(v_x, v_y) = (\frac{a\Delta t}{h}, \frac{b\Delta t}{h})$, $(Pe_x, Pe_y) = (\frac{ah}{k}, \frac{bh}{k})$ and $(R_x, R_y) = (\frac{ch}{a}, \frac{ch}{b})$.

References

[1] G.A. Baker Jr., The theory and application of the Pade approximant method, in: K.A. Brueckner (Ed.), Advances in Theoretical Physics, vol. 1, Academic Press, New York, 1965, pp. 1–58.

[2] Christopher K.W. Tam, Jay C. Webb, Dispersion-relation-preserving finite difference schemes for computational acoustics, J. Comput. Phys. 107 (1993) 262–281.

[3] I.A. Abalakin, A.V. Alexandrov, V.G. Bobkov, T.K. Kozubskaya, High accuracy methods and software development in computational aeroacoustics, J. Comput. Meth. Sci. Eng. 2 (3) (2003) 1–14.

[4] F.Q. Hu, M.Y. Hussaini, J.L. Manthey, Low-dissipation and low-dispersion Runge–Kutta schemes for computational acoustics, J. Comput. Phys. 124 (1996) 177–191.

[5] David W. Zingg, Comparison of high-accuracy finite-difference methods for linear wave propagation, SIAM J. Sci. Comput. 22 (2) (2000) 476–502.

[6] R.K. Lin, Tony W.H. Sheu, A four-step time splitting scheme for convection–diffusion equation, Numer. Heat Transfer B 45 (2004) 263–281.

[7] M.M.T. Wang, Tony W.H. Sheu, An element-by-element BICGSTAB iterative method for three-dimensional steady Navier–Stokes equations, J. Comput. Appl. Math. 79 (1997) 147–165.

[8] P.M. Gresho, R.L. Sani, On pressure boundary conditions for the incompressible Navier–Stokes equations, Int. J. Numer. Meth. Fluids 7 (1987) 1111–1145.

[9] L. Quartapelle, M. Napolitano, Integral condtions for the pressure in the computation of incompressible viscous flows, J. Comput. Phys. 62 (1986) 340–348.

[10] Chirstophe Bogry, Chirstophe Bailly, A family of low dispersive and low dissipative explicit schemes for flow and noise computations, J. Comput. Phys. 194 (2004) 194–214.

[11] T.K. Sengupta, G. Ganeriwal, S. De, Analysis of central and upwind compact schemes, J. Comput. Phys. 192 (2003) 677–694.

[12] L. Lapidus, G.F. Pinder, Numerical Solution of Paratial Differential Equations in Science and Engineering, Wiley–Interscience, New York, 1982.

[13] J. von Neumann, R.D. Richtmyer, A method for the numerical calculation on hydrodynamic shock, J. Appl. Phys. 21 (1950) 232–237.

[14] T. Meis, U. Marcowitz, Numerical Solution of Partial Differential EquationsApplied mathematical science, vol. 22, Springer, Berlin, 1981.

[15] E. Burman, P. Hansbo, Edge stabilization for Galerkin approximations of convection–diffusion-reaction problems, Comput. Meth. Appl. Mech. Eng. 193 (2004) 1437–1453.

[16] D.F. Griffiths, A.R. Mitchell, in: T.J.R. Hughes (Ed.), Finite Element for Convection Dominated Flows, AMD, vol. 34, ASME, New York, 1979, pp. 91–104.

[17] R.M. Smith, A.G. Hutton, The numerical treatment of convection – a performance comparison of current methods, Int. J. Numer. Meth. Heat Transfer 5 (1982) 439–461.
[18] Pans Tamamidis, Dennis N. Assanis, Evaluation for various high-order-accuracy schemes with and without flux limiters, Int. J. Numer. Meth. Fluids 16 (1993) 931–948.
[19] U. Ghia, K.N. Ghia, C.T. Shin, High-*Re* solutions for incompressible flow using the Navier–Stokes equations and a multigrid method, J. Comput. Phys. 48 (1982) 387–411.